

A near-infrared study of the obscured 3C129 galaxy cluster

M. Ramatsoku^{1,2,3,*}, M.A.W Verheijen¹, R.C. Kraan-Korteweg², T.H. Jarrett², K. Said⁵, and A.C. Schröder⁴

¹ Kapteyn Astronomical Institute, University of Groningen, Landleven 12, 9747 AV, Groningen, The Netherlands

² Department of Astronomy, University of Cape Town, Private Bag X3, Rondebosch 7701, South Africa

³ Department of Physics and Electronics, Rhodes University, PO Box 94, Makhanda, 6140, South Africa

⁴ South African Astronomical Observatory (SAAO), PO Box 9, 7935 Observatory, Cape Town, South Africa

⁵ School of Mathematics and Physics, University of Queensland, Brisbane, QLD 4072, Australia

Received 05 May 2020; accepted 31 August 2020

ABSTRACT

We present a catalogue of 261 new infrared selected members of the 3C 129 galaxy cluster. The cluster, located at $z \approx 0.02$, forms part of the Perseus-Pisces filament and is obscured at optical wavelengths due to its location in the zone of avoidance. We identified these galaxies using the J - and K -band imaging data provided by the UKIDSS Galactic Plane Survey within an area with a radius of 1.1° centred on the X-ray emission of the cluster at $\ell, b \approx 160.52^\circ, 0.27^\circ$. A total of 26 of the identified galaxy members have known redshifts 24 of which are from our 2016 Westerbork HI survey and two are from optical spectroscopy. An analysis of the galaxy density at the core of the 3C 129 cluster shows it to be less dense than the Coma and Norma clusters, but comparable to the galaxy density in the core of the Perseus cluster. From an assessment of the spatial and velocity distributions of the 3C 129 cluster galaxies that have redshifts, we derived a velocity of $cz = 5227 \pm 171 \text{ km s}^{-1}$ and $\sigma = 1097 \pm 252 \text{ km s}^{-1}$ for the main cluster, with a substructure in the cluster outskirts at $cz = 6923 \pm 71 \text{ km s}^{-1}$ with $\sigma = 422 \pm 100 \text{ km s}^{-1}$. The presence of this substructure is consistent with previous claims based on the X-ray analysis that the cluster is not yet virialised and may have undergone a recent merger.

Key words. atlases: catalogs: infrared - galaxies: galaxy clusters - individual

1. Introduction

At the nodes of large filamentary structures in the Universe, clusters of galaxies are continually growing and evolving as they accrete matter from the surrounding large-scale structures (Ouchi et al. 2005, Springel et al. 2005, Muldrew et al. 2015). Galaxy clusters are the largest gravitationally bound systems (Borgani et al. 2001, Allen et al. 2004, Vikhlinin et al. 2009, Mantz et al. 2010) and critical cosmological probes. Much of our present understanding on galaxy formation and evolution has been based on observing galaxies in cluster environments (Bell et al. 2004, Miller et al. 2009). Nearby galaxy clusters have particularly shaped our understanding because we are able to study them with level of detail that would not be possible for clusters at high redshifts (eg., Drinkwater et al. 2001, Chung et al. 2009, Hammer et al. 2010, Karachentsev et al. 2014, Weinzirl et al. 2014).

Our attention was drawn to the nearby 3C 129 cluster when it was uncovered as an overdensity in our Nançay HI survey of bright 2MASS Extended Sources Catalogue (2MASX; Jarrett et al. 2000) galaxies in the zone of avoidance (van Driel et al. 2009, Ramatsoku et al. 2014, KraanKorteweg et al. 2018). It is part of the expansive Perseus-Pisces supercluster (PPS) at a redshift of $z \approx 0.02$. Very little is known about this cluster's galaxy population despite being part of the well-studied PPS (Giovannelli & Haynes 1985, Haynes & Giovanelli 1986, Haynes et al. 1988, Hudson et al. 1997, Hanski et al. 2001). This is due to its location at extremely low Galactic latitudes, $\ell, b \approx 160.52^\circ, 0.27^\circ$, where severe extinction ($A_B \geq 5 \text{ mag}$) and stellar confusion in the plane of the Milky Way (MW) make locating even major overdensi-

ties in the galaxy distribution inherently difficult and unreliable (Kraan-Korteweg & Lahav 2000, Roman et al. 2000).

This galaxy cluster was first identified with the Uhuru satellite (Forman et al. 1978) in the 2–6 keV band as the X-ray source 4U 0446+44. It was subsequently observed with the ROentgen SATellite (ROSAT)¹, the European Space Agency X-ray Observatory (EXOSAT)², and the Einstein³ satellite. It was also detected and is listed in the CIZA catalogue as CIZA J0450.0+4501 (Ebeling et al. 2002). From analyses of these data, Leahy & Yin (2000) reported an X-ray temperature of $kT=5.5 \text{ keV}$, a total luminosity of $2.7 \times 10^{44} \text{ erg s}^{-1}$ in the 0.2 – 10 keV, and a total cluster mass of $4.7 \times 10^{14} M_\odot$. For comparison purposes, the Coma cluster has an X-ray temperature of 8.0 keV, a total luminosity of $7.26 \times 10^{44} \text{ erg s}^{-1}$ (Ebeling et al. 1998), and a total cluster mass of $13 \pm 2 \times 10^{14} M_\odot$ (Hughes 1989).

The cluster contains two radio galaxies, 3C 129 and 3C 129.1 ($cz = 6236$ and 6655 km s^{-1} , respectively Spinrad 1975) with jets extending far into the intra-cluster medium (ICM), as is shown in the left panel of Fig. 1. The radio galaxy 3C 129 is a well-studied head-tail radio source (Owen et al. 1979, Jaegers & de Grijp 1983, Taylor et al. 2001, Harris et al. 2002, Lal & Rao 2004, Murgia et al. 2016) with a curved tail that extends over 427 kpc (Krawczynski et al. 2003) and a total flux density of $\sim 5.3 \text{ Jy}$ at 1400 MHz (White & Becker 1992), while 3C 129.1 is a wide-angle tail radio source with a total flux density of $\sim 1.9 \text{ Jy}$ at 1400 MHz (Condon et al. 1998).

¹ <https://heasarc.gsfc.nasa.gov/docs/rosat/rosat3.html>

² <https://heasarc.gsfc.nasa.gov/docs/exosat/exosat.html>

³ https://heasarc.gsfc.nasa.gov/docs/einstein/hea02_about.html

* m.ramatsoku@ru.ac.za

Due to the high extinction layer of the Milky Way, most of what is known about the cluster is based on its X-ray and radio source properties; its constituent galaxies had not been observed before. For this reason we decided to perform a census of the galaxy population of this cluster by conducting a deep, blind, HI imaging survey with the Westerbork Synthesis Radio Telescope⁴ (WSRT). This was done using a mosaic of about $3^\circ \times 3^\circ$ covering the cluster and its immediate surrounding regions of the PPS (see Ramatsoku et al. 2016 hereafter paper1).

Our aims are to investigate the large-scale and sub-structure associated with the 3C 129 galaxy cluster and to determine its relevance to flow fields around the larger PPS environment. As evident in the 2MASS survey of extended sources, this large-scale structure envelops the cluster as it crosses from the southern to northern Galactic hemispheres (Jarrett 2004) (see the right panel of Fig. 1). Our data will also aid in efforts of the 2MASS Tully-Fisher survey (2MTF; Masters et al. 2008) since we cover the inner ZoA regions ($b \approx |5^\circ|$) which are excluded by this survey. Moreover, since we covered a wide area of the cluster with our HI imaging survey, we will be able to characterise the various environments in and around the cluster to study the environmental effects on the population of galaxies therein.

HI is an ideal diagnostic tool for studying processes in clusters because of its sensitivity to the environment. It has also proved most effective at detecting galaxies at low Galactic latitudes (Kraan-Korteweg et al. 1994, van Driel et al. 2009, Henning et al. 2010, McIntyre et al. 2015, Staveley-Smith et al. 2016, Sanchez-Barrantes et al. 2019). However, it is unsuitable for tracing the dominant galaxy population of clusters which primarily comprises gas-poor, early-type galaxies. These early-type galaxies stand out at near-infrared wavelengths, particularly in the *J* and *K* bands. Combining the HI and NIR data provides a versatile and robust tool for conducting an inventory of the galaxy population in clusters, particularly behind the Galactic Plane (GP) where dust extinction presents a challenge for optical wavelengths.

In this paper we explore the NIR colour-magnitude properties of galaxies within the observed WSRT HI mosaic to identify cluster members of the 3C 129 cluster, and to complement our HI detections at NIR wavelengths. This is achieved using data from the UKIDSS Galactic Plane Survey (Lucas et al. 2008).

The layout of the paper is as follows; in Sect. 2 we give a summary of the HI sample and discuss the near-infrared photometry of the UKIDSS images. The colour-magnitude relation and cluster membership selection are discussed in Sect. 3. A subset of the catalogue of the cluster galaxies and images are described and presented in Sect. 3.2.1, with the full catalogue and images given in Appendix B. The near-infrared properties of the 3C129 cluster are discussed in Sect. 3.2.3 and are compared with those of other galaxy clusters nearby. We describe the structure of the cluster in Sect. 4.1 and give a summary of the main results in Sect. 5. We assume a Λ cold dark matter cosmology with $\Omega_M = 0.3$, $\Lambda_\Omega = 0.7$ and a Hubble constant $H_0 = 70 \text{ km s}^{-1} \text{ Mpc}^{-1}$ throughout this paper.

2. Data samples

2.1. The HI data

For a detailed description of the WSRT HI survey in and around the 3C 129 cluster, we refer the reader to paper1. Here, only a brief summary is provided below:

⁴ <http://www.astron.nl/radio-observatory/>

The 21 cm HI-line imaging survey was conducted using the WSRT comprising 35 pointings each with an integration time of 12 hours, in a hexagonal mosaic centred at $\ell, b \approx 160^\circ, 0.5^\circ$ (see Fig. 2) which is where the Perseus-Pisces supercluster crosses the zone of avoidance. The total sky area covered was $\sim 9.6 \text{ deg}^2$, with a survey rms sensitivity of 0.36 mJy/beam over the radial velocity range of $cz = 2400 - 16600 \text{ km s}^{-1}$, with 16.5 km s^{-1} and $23'' \times 16''$ velocity and angular resolution respectively. We detected a total of 214 HI galaxies over the entire radial velocity range, with HI masses between $5 \times 10^7 - 2 \times 10^{10} M_\odot$ of which 80 were spatially resolved. In total 87 were detected at a redshift of the 3C 129 cluster ($cz \sim 4000 - 8000 \text{ km s}^{-1}$) with 24 within its radius (see Sec. 3.1 for how we define the radius of the cluster). The rest were found in the foreground and background of the cluster, at redshifts of, $cz = 2400 - 4000 \text{ km s}^{-1}$ and $cz \sim 10000 - 16600 \text{ km s}^{-1}$, respectively. The footprint of our HI observations is shown in blue in Fig. 2.

2.2. The near-infrared data

The cluster is prominent in the 2MASX catalogue as illustrated in the right panel of Fig. 1. However, we extracted our near-infrared sample of galaxies from images provided by the UKIRT Infrared Deep Sky Survey (UKIDSS: Lawrence et al. 2007) because of its improved depth and spatial resolution. We used Data Release 10 (DR10) of a sub-survey of UKIDSS, the Galactic Plane Survey (GPS), which covers an area of 1800 deg^2 to a 5σ *K* ($2.2\mu\text{m}$)-band depth of 18.8 mag (Vega)(Lucas et al. 2008). The UKIDSS-GPS with a pixel scale of $0.2''/\text{pix}$ (after microstepping) and an average seeing of $0.8''$ is highly successful at separating stars from galaxies further from the Galactic mid-plane ($|b| \gtrsim 5^\circ$). However, it suffers some confusion at lower Galactic latitudes. At these latitudes visual inspection is still a superior method for identifying galaxies (Lucas et al. 2008).

Given the large area covered by our WSRT mosaic it was not possible to visually inspect the entire region. For this reason we opted to employ intermediary steps prior to visual inspection. We started by conducting source detection using the SExtractor software (SEXTRACTOR version 2.8.6; Bertin & Arnouts 1996). The detection and extraction of sources was conducted over sixteen overlapping UKIDSS-GPS images of size $1^\circ \times 1^\circ$, supplemented by smaller images ($\sim 30' \times 30'$) which together cover the entire HI mosaic survey footprint of the WSRT (see Fig. 2). We used the *K*-band for source detection since it is least affected by Galactic dust extinction, and provides higher signal-to-noise ratios compared to the *J* ($1.2\mu\text{m}$)- or *H* ($1.6\mu\text{m}$)-bands.

The source detection performed by SEXTRACTOR uses an algorithm that registers a detection when a set number of pixels are connected as specified by the detection parameters, DETECT_MINAREA and DETECT_THRESH. The GLOBAL background noise was estimated using a small mesh set by BACK_SIZE = 64. This size was chosen to prevent an overestimation of the background due to wings of very bright sources. To set the detection parameters, a two-fold approach was adopted; for sources with pixel values above 9σ , a minimum of 10 adjacent pixels was required, and sources between $3\sigma - 9\sigma$ were only accepted if they had a minimum of 50 adjacent pixels.

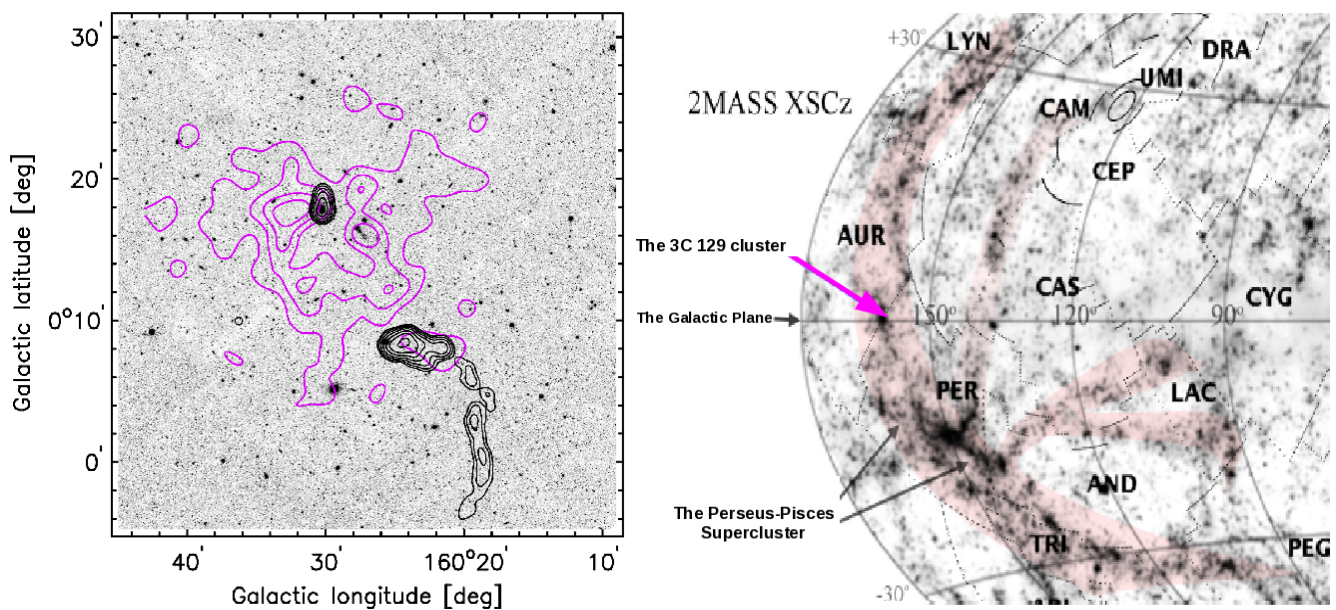


Fig. 1: Left panel: The central region of the 3C 129 cluster ($\sim 37' \times 37'$) showing the K -band UKIDSS image. The VLA 1424 MHz contours of the radio sources (NVSS; Condon et al. 1998) are overlaid in black. 3C 129 is the head-tailed source with a curved tail on the right and the wide-angle tailed radio source on the left is 3C 129.1. The X-ray 0.1 - 2.4 keV emission from ROSAT is overlaid in magenta. Right panel: An Aitoff Galactic projection of the galaxy distribution extracted from the 2MASS Galaxy Catalog (XSCz) in the Local Universe shown from the northern hemisphere (Jarrett 2004). The image highlights the large filamentary structure of the PPS shaded in pink. The 3C 129 cluster lies in the GP crossing at $\ell \approx 161^\circ$.

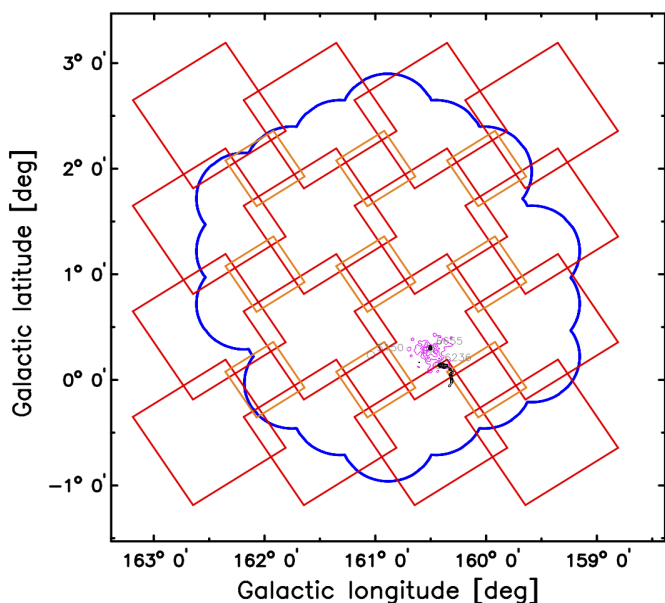


Fig. 2: The projected sky distribution of the observed WSRT hexagonal mosaic in blue. Coverage of the near-infrared tiles from the UKIDSS - GPS data is outlined in red. The X-ray emission is shown in magenta and the position of the contours of the radio sources 3C 129 and 3C 129.1 are shown in black.

Once the sources were detected, we conducted a deblending procedure to separate objects that were recognised as connected on the sky using the deblending parameters with $\text{DEBLEND_MINCONT} = 0.001$ and $\text{DEBLEND_NTHRESH} = 32$. Values for these parameters were chosen after performing tests with a wide range of values and verifying results by visual inspection to en-

sure that spurious detections were minimised and that no obvious sources were missed. In Table A.1, we provide a summary of the `SEXTRACTOR` parameters we adopted for detecting sources in the UKIDSS-GPS K -band images.

2.3. Star-galaxy separation

Although `SEXTRACTOR` parameters described in section 2.2 were optimised to limit the number of stars and spurious detections, the high stellar density in the GP necessitated further processing to separate the stars from galaxies. In this section we describe the three-step process that was conducted for this purpose.

2.3.1. `SEXTRACTOR` stellarity index

Firstly, we performed a preliminary star-galaxy classification using `SEXTRACTOR`'s stellarity index (`CLASS_STAR`). This is a dimensionless parameter that characterises objects as either point-like or extended. This parameter is based on a neural-network analysis approach that compares the point spread function to the object scale and then provides a confidence level estimate of the classification which ranges from 0 for galaxies to 1 for stars. Figure 3 shows the distribution of the `CLASS_STAR` values of all sources which were detected using procedures described in Sect. 2.2. From this plot two distinct populations with `CLASS_STAR` values of 0 and 1 are evident. Moreover, the distribution of sources classified as galaxies shows a sharp decline from `CLASS_STAR` = 0.0 to 0.35, it then flattens and rises steeply from `CLASS_STAR` = 0.8 to 1.0. Based on the distribution of the stellarity index, `CLASS_STAR`, we classified sources as:

Galaxies; $\text{CLASS_STAR} \leq 0.35$.

Stars or galaxies; $0.35 < \text{CLASS_STAR} < 0.8$.

Stars; $\text{CLASS_STAR} \geq 0.8$.

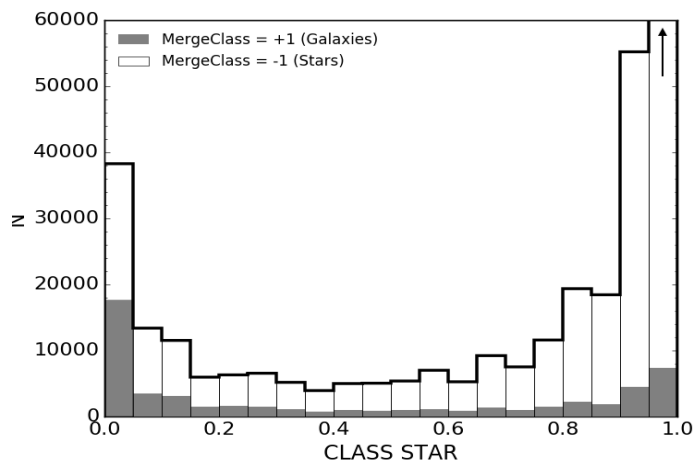


Fig. 3: The distribution of `SEXTRACTOR` stellerity index, `CLASS_STAR` of all objects found in the UKIDSS-GPS searched images. All objects with `CLASS_STAR > 0.8` are stars, those with `CLASS_STAR < 0.35`, galaxies and $0.35 < \text{CLASS_STAR} < 0.8$ are ambiguous objects. The open histogram shows the distribution of objected labelled as stars in the UKIDSS catalogue (`MERGECLASS=-1`) and the filled histogram are those labelled as galaxies (`MERGECLASS=+1`). The horizontal arrow points to a higher number count of $\sim 10^5$ in that bin that is not shown in the plot.

2.3.2. UKIDSS-GPS star-galaxy separator

Secondly, we validated objects classified as galaxies by `CLASS_STAR` by cross-correlating them with the UKIDSS-GPS catalogue which also provides a star-galaxy classification parameter, `MERGECLASS`. This parameter is based on quantitative measurements in the *J*, *H* and *K* passbands of the observed radial profiles by the UKIDSS data reduction pipeline (Dye et al. 2006). The profiles are characterised by the ‘mergeClass-Stat’ parameter and identified as either point-like, resolved or artefacts. Resolved sources are assigned large ‘mergeClassStat’ values, while smaller values are associated with point-like sources. Moreover, the UKIDSS-GPS further separates galaxies from stars by making cuts based on the difference between their Petrosian (resolved) magnitude and the point source magnitude (Lucas et al. 2008). In this catalogue galaxies are assigned `MERGECLASS= +1` and stars are assigned `MERGECLASS= -1`.

2.3.3. Visual inspection

We found that the `CLASS_STAR` and `MERGECLASS` parameters are not reliable under all circumstances. For instance, out of all sources with `CLASS_STAR = 0.0` only about 47% were classified as galaxies by `MERGECLASS` (see Fig. 3). Because of this, we needed to ensure that galaxies were not missed based on these parameters, particularly in the ambiguous $0.35 < \text{CLASS_STAR} < 0.8$ range. This necessitated a further visual inspection step to improve the classification of each object, and to remove any spurious detections. This was done for all objects with `CLASS_STAR < 0.8` and `MERGECLASS = +1` and `MERGECLASS = -1`, those with `CLASS_STAR > 0.8` were not inspected visually since

only 0.05% of the objects in these bins had `MERGECLASS = +1`. We conducted the visual inspection using `ds9` on the *J*, *H* and *K* bands three-colour (RGB) composite images from UKIDSS. The extended nature of galaxies and their colour made them readily distinguishable in this manner.

After removing artefacts, stars and duplicate detections in overlapping regions of the UKIDSS images, the final sample consisted of 9737 unique galaxies spatially distributed over the full WSRT mosaic. In section 3.1, we give a full description of how we selected galaxies belonging to the 3C 129 cluster.

2.4. Star subtraction

Due to the high stellar density at low Galactic latitudes, images required additional steps to remove stars superimposed on the galaxies to obtain accurate photometry. We conducted this by fitting a point-spread function (PSF) to stars and subsequently removed them from the galaxy. For this purpose we used a four-step script based on the `IRAF` routine `KILLALL` (Buta & McCall 1999), which in turn is based on `DAOPHOT` tasks (Stetson 1987). The four steps were as follows: (a) We used `IMSTAT` to determine the rms and sky background in the image; (b) modelled the galaxy using `ELLIPSE` and `BMODEL`, and removed this model from the image. It should however, be noted that galaxy structures such as spiral arms may be not be modelled fully and might result in residuals in the galaxy-subtracted image; (c) used `SEXTRACTOR` to detect bright stars that are above 3.5σ in the image in which the galaxy has been subtracted. The PSF photometry of these sources was then determined using `DAOPHOT` (tasks `ALLSTAR` and `PHOT`) and removed from the image. This step was repeated for fainter stars above 1.8σ . To mitigate against misidentifying residual structures as stars, we required these stars to be detected by `DAOFIND` at the 2σ threshold; (d) the two lists with the bright and faint stars were combined and removed from the original image using the `SUBSTAR` task; (e) residuals resulting from imperfect PSF fits to stars in the image were found and removed. We repeated steps (b) to (e) four times, each time improving the galaxy model, which resulted in a more reliable star removal.

Figure 4 shows example images for three galaxies in our sample before (left panel) and after (right panel) star-subtraction. It illustrates that this star removal procedure performs quite well. In fact, it has been shown by Woudt et al. (2005) and Mutabazi et al. (2014), through simulations of subtracting artificial stars added to non-crowded fields, that removing stars this way has a minimal effect (less than 0.01 mag on average) on the galaxy photometry.

2.5. The NIR photometry

After subtracting all the stars we extracted the galaxy photometric parameters. Since UKIDSS photometric parameters are only measured within circular apertures which are inadequate for elongated galaxies, we used customised python scripts developed by K. Said⁵ and W. Williams⁶ based on a combination of `SEXTRACTOR` and `IRAF` tasks.

⁵ khaled.said@anu.edu.au

⁶ w.williams@strw.leidenuniv.nl

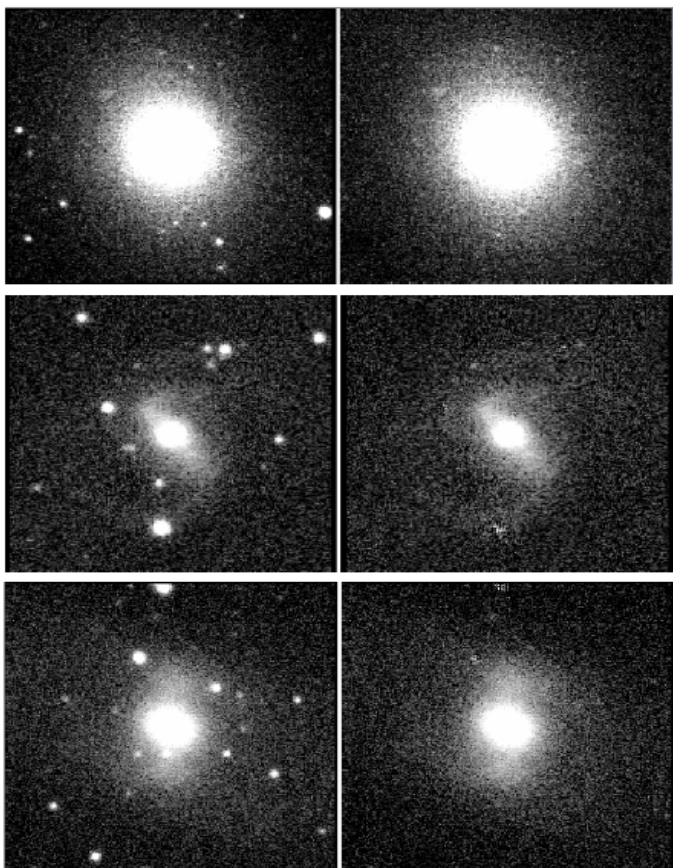


Fig. 4: Postage stamp examples of K -band images of galaxies before (left panels) and after star-subtraction (right panels).

2.5.1. Astrometry of positions

First, the central positions of galaxies were determined by adding the three images from the $J+H+K$ bands and measuring the intensity-weighted centroid. This method of determining positions is more accurate as it measures the centre of the galaxy from higher signal-to-noise images (Jarrett et al. 2000).

2.5.2. Ellipticities and geometries

Next, ellipticities and position angles were determined individually from the J , H and K band images. The IRAF task ELLIPSE was used to fit ellipses to the galaxy image. Ellipticities, $\epsilon = (1 - b/a)$ and position angles (ϕ ; counter clockwise from north) were then fitted at semi-major axis intervals, while keeping the central coordinates, X and Y fixed. The ELLIPSE task produced tables containing the intensity (in counts) within the ellipse and the ellipticity and position angle at each semi-major axis interval including their errors. Then the galaxy's position angle and ellipticity were determined to be the average value in the outer disc between $1\sigma - 2\sigma$ isophotes, where σ is the sky background rms.

2.5.3. Magnitudes

Finally, the isophotal magnitudes were measured within elliptical apertures in all bands (J , H , K). The K -band surface brightness $\mu = 20$ mag arcsec $^{-2}$ isophote was adopted to determine the isophotal radius ($r_{K_{20}}$). Fiducial magnitudes were measured within this same aperture of radius $r_{K_{20}}$ for the J , H , K -bands. All the magnitudes are based on the Vega calibration.

2.6. Photometric checks

To check our photometric consistency, we derived from the UKIDSS images galaxy magnitudes within a $7''$ radius circular aperture and compared these with their counterparts in the 2MASX catalogue (Jarrett et al. 2000) in the same $7''$ circular aperture. Sources in both catalogues were matched if they were separated by less than $1.5''$. We used this small correlation radius of $1.5''$ because the UKIDSS WFCAM astrometric calibration was derived from 2MASS (Hodgkin et al. 2009), which has a positional accuracy of about $0.5''$. Only galaxies with reliable photometry (as flagged in the 2MASX catalogue) were compared. We found 363 counterparts in the 2MASX catalogue.

In Fig. 5, we show a comparison of our UKIDSS photometry with that of the 2MASX. The comparison relation used is:

$$\Delta m = m_{2MASX} - m_{UKIDSS}. \quad (1)$$

By this equation, a positive Δm indicates that 2MASX magnitudes are fainter than our UKIDSS magnitudes. The offsets given in the top right corners of Fig. 5 indicate that the 2MASX galaxies are slightly brighter than their UKIDSS counterparts. These offsets can be attributed to the 2MASX low angular resolution ($\sim 2.0''$), that cannot resolve the sources. The improved resolution of the UKIDSS ($\sim 0.8''$) on the other hand allows for the detection and subtraction of fainter foreground stars that would otherwise contribute to the galaxy's brightness within the measurement aperture. Moreover the different filters may also have contributed to slight offsets because the UKIDSS uses the Mauna Kea Observatory (MKO; Hodgkin et al. 2009) filter set which is slightly different from the 2MASS filter set (Cohen et al. 2003).

2.7. Extinction

Galaxies in the ZoA tend to have their brightness reduced due to the dust obscuration in the Milky Way. This effect is less prominent in the near-infrared compared to the optical, but it is nonetheless not negligible. Within our WSRT field the Galactic extinction values range from $A_K = 0.16 - 0.56$ mag (see Fig. 7 of paper I).

We correct for this effect using the extinction law;

$$\frac{A_\lambda}{E(B - V)} = R_\lambda, \quad (2)$$

where A_λ is the extinction in a given band and $E(B - V)$ is the colour reddening from Schlegel et al. (1998) with the Schlafly & Finkbeiner (2011) correction factor of 0.86 applied. The value for $R_V = 3.1$ is given by Schlegel et al. (1998). Using the parametrisation by Fitzpatrick (1999) we derive the extinction in the J , H and K bands to be,

$$A_J = 0.741E(B - V), \quad (3)$$

$$A_H = 0.456E(B - V), \quad (4)$$

$$A_K = 0.310E(B - V). \quad (5)$$

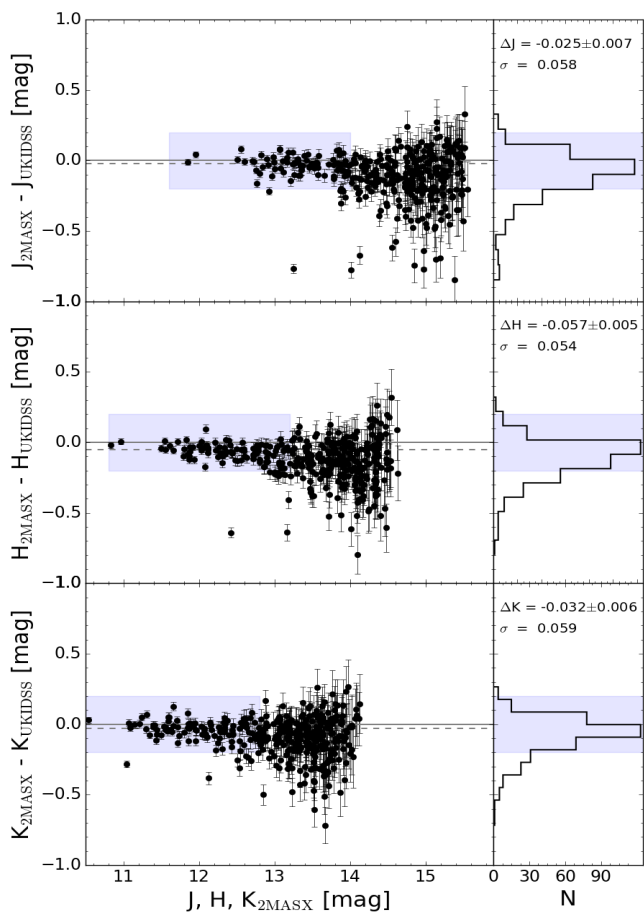


Fig. 5: Comparison between the 2MASX and UKIDSS circular aperture magnitudes measured within a $7''$ radius for the J (top), H (middle) and K (bottom) bands. The median offset between the two surveys is indicated by the dashed line, it is printed in the top right legend. This median was determined within areas marked by the blue shades also marked in the histograms.

The effect of extinction on our galaxies is low given that our field has a median extinction of $A_K = 0.29 \pm 0.05$ mag, however this is not negligible. This extinction also translates into a reduction of the isophotal radius of the galaxy due to the loss of the fainter, low surface brightness outer regions. According to Riad et al. (2010) extinction at for example, $A_K = 1.0$ mag can reduce the isophotal radius by $\sim 28\%$.

3. The colour-magnitude relation

The colour-magnitude relation (CMR) has been shown to be a powerful technique for selecting galaxies in clusters since they form a distinct linear feature in the colour-magnitude diagram (Visvanathan & Sandage 1977). This feature, known as the red sequence is typically composed of passive early-type galaxies with old stellar populations. It is not yet clear when in the history of the Universe the red sequence emerged, however, several studies have shown that it is present at all redshifts up to $z \sim 1$ (Bell et al. 2004, Menci et al. 2005, Scarlata et al. 2007, Mei et al. 2009). Great efforts have been taken with spectroscopic and photometric surveys to push the redshift limit further. Several massive red galaxies have been detected at high redshifts through these studies, however, they are often constrained by low sample numbers in the case of the former, while the latter suffers uncer-

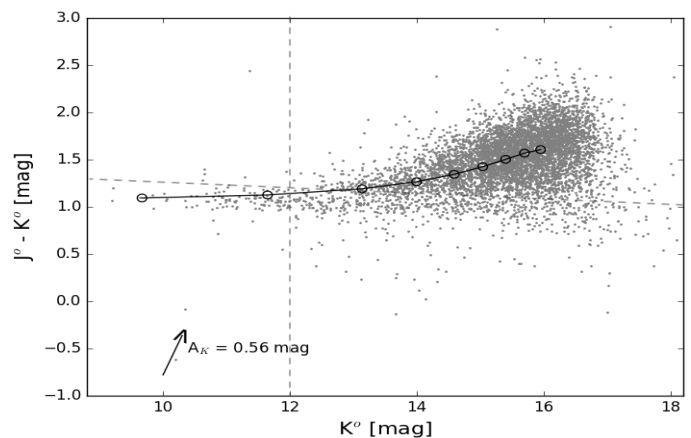


Fig. 6: The colour-magnitude diagram of 9737 sources from the UKIDSS-GPS within the WSRT mosaic (see Sect. 2.2). The reddening curve computed from redshift $z = 0.02$ to $z = 0.4$ is shown by the black line with open circles representing the redshift bin and the Galactic dust reddening vector for a K -band extinction of 0.56 mag is indicated with the arrow. Dashed lines represent the boundaries of red sequence cluster members compared to blue outliers (vertical line) or background galaxies (slanted line).

tainties in the rest-frame colour measurements at high redshifts resulting in a large scatter on the CMR and less-defined red sequence (Cirasuolo et al. 2007, Franzetti et al. 2007, Cassata et al. 2008, Taylor et al. 2009, Tanaka et al. 2010, Spitler et al. 2012). Regardless of these limitations, when the red sequence has been clearly observed, it has a well-defined slope that evolves with redshift and a small (< 0.1 mag) intrinsic scatter (Bower et al. 1992, Gladders et al. 1998, López-Cruz et al. 2004, Stott et al. 2009).

In addition to the tight CMR, galaxies in regular clusters have a radial distribution that is typically centrally concentrated (Dressler 1980). They also form the dominant population at the bright end of the galaxy luminosity function and create a high contrast against the background, thus making them easily recognisable in surveys (Gladders et al. 1998).

Given the scarcity of redshift information of galaxies in the 3C 129 cluster we use the CMR in the near-infrared to identify cluster members because most galaxies are invisible at the optical wavelength due to extinction in this region. We use the red sequence feature in the CMR as well as the angular on-sky projection distribution to detect clustering. The advantage of using this technique is that it is not affected by projection effects since any random distribution of galaxies will not form a coherent red sequence signature in the colour-magnitude diagram.

In Fig. 6 we present the NIR colour-magnitude diagram (CMD) of all 9737 galaxies within the observed WSRT mosaic (see Fig. 2). Colours were measured inside the $\mu_k = 20$ mag arcsec $^{-2}$ fiducial isophotal aperture defined in the K -band and corrected for foreground extinction based on the DIRBE/IRAS maps as described in Sect. 2.7.

Two well-defined populations are apparent in this plot. The dominant population ($K^o > 12$ mag, $J^o - K^o \gtrsim 1.3$ mag) con-

sists of redshifted background galaxies. The overlaid reddening curve⁷ (Chilingarian et al. 2010) supports this claim. The other identifiable population is a slightly slanted band of galaxies that stretches between $8 \lesssim K \lesssim 16$ mag with colours, $J^o - K^o \approx 1.1$ mag. This second feature contains within it the red sequence of the 3C 129 cluster. Below the red sequence is a small population of blue outliers which were visually inspected and found to be close binary stars and/or artefacts that were missed during the star-galaxy separation process in the UKIDSS images (see Sect. 2.3).

3.1. The red sequence and cluster membership

To determine the galaxy cluster membership we used a three step process;

Firstly, a region of the CMD containing the red sequence was selected and an estimate of the initial fit was made by visual inspection. All points deviating by more than 3σ from this initial fit were removed from the full sample. We then performed an iterative linear fit of the form, $J - K = \alpha K + c$ where the slope of the red sequence is denoted by α to points that were within $\pm 3\sigma$ of the initial fit. The final fit gives $(J - K)^o = -(0.023 \pm 0.002)K^o + 1.25$ with a 1σ dispersion of 0.039 mag. The slope matches that of the Coma cluster of $\alpha = -0.017 \pm 0.009$ (measured by Stott et al. 2009), which is at a similar redshift of $z \approx 0.02$ as the 3C 129 cluster. The $J - K$ colours of the red sequences are also comparable to that of galaxy clusters in the Wide-field Nearby Galaxy-cluster Survey (WINGS: Valentinuzzi et al. 2011). Galaxies within $\pm 3\sigma$ of the final fit formed the initial list of the cluster member candidates.

Secondly, we limited the relative background contamination in the initial sample list of red sequence galaxies by only selecting galaxies with $r_{K_{20}} > 3''$. For galaxies with $r_{K_{20}} > 3''$ the red sequence becomes increasingly contaminated by background galaxies which are hard to discriminate from true cluster members. Moreover, at these sizes cluster members will fall in the dwarf regime and are of no interest to this study, and fall below the cluster completeness limit of $K^o \approx 15.0$ mag or ($M_K \approx -19.7$ mag; see Sect. 3.2.1).

Thirdly, we defined a radius r_{cl} of the cluster centred on the ROSAT X-ray emission. This cluster radius was chosen based on the spatial distribution (cf. Fig. 13) of the red sequence galaxies which have radii larger than $r_{K_{20}} > 3''$ out to where they became sparsely distributed. Assuming a redshift of $z = 0.02$ the radius was found to be $r_{cl} \approx 1.7$ Mpc ($\sim 0.8r_A$)⁸. It corresponds to about $1.34R_{200}$, where R_{200} is the radius at which the average interior density of the cluster is $200 \times \rho_c$, and ρ_c is the critical density of the Universe. The R_{200} of the 3C 129 cluster is ~ 1.24 Mpc based on the 0.1 – 2.4 keV band measurements by ROSAT (Piffaretti et al. 2011). We therefore only selected red sequence galaxies within $r_{cl} < 1.34R_{200}$ as potential cluster members.

After applying the steps outlined above, we obtained a sample of 250 galaxy members of the 3C 129 cluster which lie on the red-sequence. Of these galaxies, 13 were already detected in our HI survey (Ramatsoku et al. 2016). The CMD of all galaxies on the red sequence is shown in Fig 7. In addition, we included 11

more galaxies with $r_{K_{20}} < 3''$ that were detected in HI within the velocity window and the defined radius of the cluster on the sky regardless of their location on the red-sequence. Thus the final sample of the 3C 129 cluster members comprises 261 galaxies.

We note that we cannot measure the contamination of the final sample by background galaxies without redshift measurements. However, it has been previously shown that this method of finding galaxy cluster members in both the infrared and optical wavelengths results in a background contamination of less than 5% (Gladders & Yee 2000).

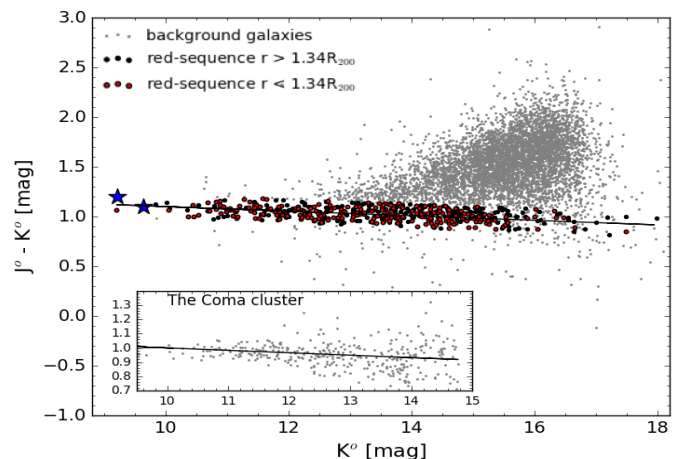


Fig. 7: The colour-magnitude diagram showing the red sequence signature of the 3C 129 cluster in red with the two blue stars identifying the bright radio sources, 3C 129 and 3C 129.1. The fitted slope, $\alpha = -0.023 \pm 0.002$ mag of the cluster is illustrated by the black solid line and compared to that of the Coma cluster using 2MASX data in the inserted CMD. Black points are galaxies outside the cluster radius of $r_{cl} < 1.34R_{200}$ and grey points are mostly background galaxies.

3.2. Morphologies of the cluster members

Figure 8 shows the CMD of the cluster with galaxies separated into approximate morphologies based on a visual inspection and a subjective estimate of their bulge-to-disc ratios, their ellipticities and compactness. The morphological classification was independently conducted and adjudicated by co-authors. This classification is only meant to distinguish large-scale trends and to give a general description of galaxy morphologies in the cluster. Galaxies were classified into five broad groups of early-types (E/S0), early spirals (eS) such as Sa/Sb, medium spirals (mS) which were typically of Sc/Sd type, the late-type spirals (lS) which were mostly Sdm, and Irregular (Irr) galaxies without any discernible structure. In this plot we also indicate with black squares, the galaxies detected in HI (with UKIDSS counterparts) within the velocity range and radius of the cluster.

From Fig. 8 we find that early-type galaxies (E/S0) and the early-spirals are mostly located at the bright end of the red sequence. This is to be expected given that we are evaluating a potentially rich cluster which tends to have a higher fraction of these bright early-type galaxies than star forming late-type galaxies.

The mid-range spiral galaxies (mS) show no obvious trends in the CMD except that they are predominantly at fainter magnitudes compared to the early-type galaxies. There is a number

⁷ <http://kcor.sai.msu.ru>

⁸ r_A is the Abell radius

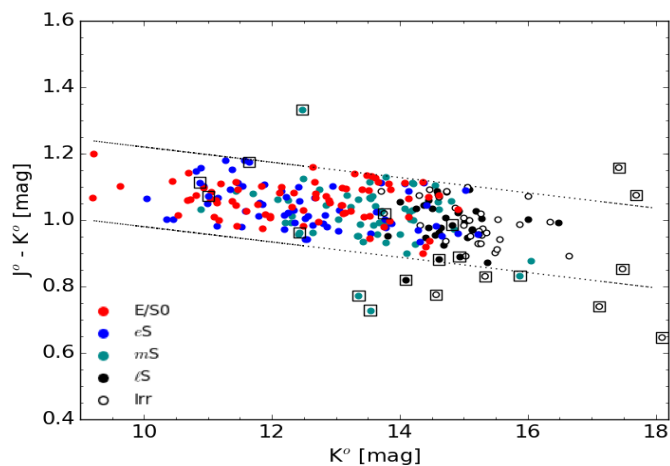


Fig. 8: The CMD of the 3C 129 cluster identified as members. Colours indicate morphological type. Circles are the red-sequence galaxies, and those enclosed in squares are HI detected galaxies within the radius and velocity range of the cluster. The dotted lines show the $\pm 3\sigma$ rms dispersion (0.12 mag) from the fitted red sequence relation: $J - K = -0.023K + 1.25$.

of these type of galaxies ($\sim 23\%$) detected near the centre of the cluster (see also Figs. 13 and 14 in Sect. 4). Interestingly, they were not detected in HI, suggesting they might be stripped of their gas by ram-pressure from the ICM upon infall, and are HI deficient. Judging by their morphologies alone, these should have otherwise been detected in our HI observations.

Late-type spirals and irregular galaxies are mostly found at the faint end of the CMD, that is, at $K^o \gtrsim 14$ mag. These are typically LSB galaxies which could have lost their gas through tidal stripping or interaction with the ICM (Conselice et al. 2003). On the other hand, most of the HI detected galaxies also populate this end of the CMD, but tend to be slightly bluer ($J^o - K^o \lesssim 1.0$ mag) than their LSB counterparts. They are located in the cluster outskirts where we expect less interaction and where we expect galaxies to have retained their gas.

Analyses of these populations of galaxies as well as the effect of the various environments in which they reside, requires a more comprehensive analysis than presented in this paper. Here we only present a first description. We will study and discuss the detailed nature of these galaxies in the forthcoming paper III.

3.2.1. The catalogue of candidate cluster galaxies

A full catalogue of the 261 cluster members is presented in Appendix B, Table B. Galaxies are listed in ascending order of their K -band magnitudes (from the brightest to the faintest). For each galaxy a $1.2' \times 1.2'$ image in the J, H and K band was extracted. The false colour (RGB) postage stamps of these images are shown in Fig. B in the same order as the catalogue. Galaxy morphologies are printed at the bottom of the images. The galaxies that were detected in HI are framed in cyan. The first 30 entries of the catalogue and their corresponding images are shown in Table. 1 and Fig 9, respectively.

Table 1: Near-infrared parameters of the first 30 entries of 3C 129 candidate cluster galaxies. The full catalogue is available in Appendix B

ID no.	Unique ID	RA	Dec	ℓ	b	ϵ_K	ϕ_K	r_{K20}	J_{K20}	H_{K20}	K_{20}	$E(B-V)$	J^0-K^0	Type	v_{rad}
	ZoA	deg	deg	deg	deg		deg	"	mag	mag	mag	mag	mag		km s ⁻¹
(1)	(2)	(3)	(4)	(5)	(6)	(7)	(8)	(9)	(10)	(11)	(12)	(13)	(14)	(15)	(16)
1	J044908.26+445540.3	72.284	44.928	160.490	0.086	0.17	24.71	28.10	10.96 ± 0.02	9.94 ± 0.02	9.51 ± 0.02	0.89	1.07	E/S0	—
2	J045006.67+450305.8	72.528	45.052	160.505	0.298	0.20	65.00	37.30	11.21 ± 0.04	10.10 ± 0.04	9.59 ± 0.04	0.98	1.20	E/S0	6655*
3	J044909.06+450039.4	72.288	45.011	160.427	0.142	0.10	-60.00	25.60	11.50 ± 0.03	10.46 ± 0.04	10.00 ± 0.04	0.94	1.10	E/S0	6236 ^x
4	J045145.56+443602.6	72.940	44.601	161.039	0.235	0.40	60.00	22.80	11.75 ± 0.03	10.82 ± 0.03	10.35 ± 0.04	0.79	1.07	eS	5086 ⁺
5	J044939.78+440922.1	72.416	44.156	161.141	-0.337	0.09	-55.01	12.79	12.05 ± 0.02	11.16 ± 0.02	10.76 ± 0.02	0.65	1.01	E/S0	—
6	J044842.39+454818.5	72.177	45.805	159.769	0.593	0.40	-61.15	21.62	12.25 ± 0.02	11.23 ± 0.02	10.77 ± 0.02	1.12	1.00	eS	—
7	J045245.69+450106.2	73.190	45.018	160.829	0.638	0.44	85.11	19.63	12.31 ± 0.02	11.23 ± 0.02	10.78 ± 0.02	0.94	1.12	E/S0	—
8	J045219.88+451546.1	73.083	45.263	160.592	0.734	0.50	-60.00	25.90	12.23 ± 0.05	11.26 ± 0.05	10.83 ± 0.06	0.91	1.00	eS	—
9	J045326.75+441900.7	73.361	44.317	161.449	0.288	0.06	26.77	14.31	12.32 ± 0.02	11.38 ± 0.02	10.96 ± 0.02	0.69	1.06	E/S0	—
10	J045045.92+450659.7	72.691	45.117	160.529	0.428	0.27	0.36	13.39	12.62 ± 0.02	11.56 ± 0.02	11.05 ± 0.02	1.00	1.14	E/S0	—
11	J044719.31+441701.6	71.830	44.284	160.774	-0.576	0.47	-73.54	16.96	12.50 ± 0.02	11.56 ± 0.02	11.06 ± 0.02	0.69	1.15	eS	4993
12	J044843.25+445216.0	72.180	44.871	160.486	-0.007	0.11	32.33	9.98	12.54 ± 0.02	11.54 ± 0.02	11.11 ± 0.02	0.84	1.07	E/S0	—
13	J044459.45+453344.1	71.248	45.562	159.534	-0.059	0.30	-23.53	14.62	12.83 ± 0.02	11.73 ± 0.02	11.19 ± 0.02	1.35	1.06	E/S0	—
14	J044429.89+442914.8	71.125	44.487	160.291	-0.827	0.31	44.80	14.65	12.81 ± 0.02	11.78 ± 0.02	11.23 ± 0.02	0.98	1.16	eS	—
15	J044724.21+445928.3	71.851	44.991	160.244	-0.107	0.80	-35.00	31.50	12.64 ± 0.05	11.67 ± 0.05	11.25 ± 0.07	0.84	1.03	mS	—
16	J045414.90+450315.1	73.562	45.054	160.967	0.864	0.17	-41.28	19.00	12.79 ± 0.02	11.75 ± 0.02	11.29 ± 0.02	0.93	1.10	eS	6269
17	J045129.31+451852.0	72.872	45.314	160.458	0.652	0.57	-35.96	17.04	12.86 ± 0.02	11.84 ± 0.02	11.31 ± 0.02	1.04	1.10	E/S0	—
18	J045028.01+443407.6	72.617	44.569	160.916	0.037	0.70	-74.56	15.98	12.74 ± 0.02	11.79 ± 0.02	11.32 ± 0.02	0.80	1.07	E/S0	—
19	J045156.57+445815.0	72.986	44.971	160.774	0.496	0.47	-12.60	14.73	12.79 ± 0.02	11.79 ± 0.02	11.33 ± 0.02	0.94	1.05	eS	—
20	J045251.94+444122.5	73.216	44.690	161.095	0.443	0.56	63.37	16.94	12.90 ± 0.02	11.92 ± 0.02	11.47 ± 0.02	0.85	1.07	eS	—
21	J045018.46+454152.2	72.577	45.698	160.031	0.738	0.27	24.97	12.06	13.08 ± 0.02	11.99 ± 0.02	11.49 ± 0.02	1.17	1.08	E/S0	—
22	J045324.45+451127.6	73.352	45.191	160.768	0.835	0.40	29.03	12.08	12.97 ± 0.02	11.93 ± 0.02	11.50 ± 0.02	0.98	1.05	E/S0	—
23	J044753.50+443250.9	71.973	44.547	160.638	-0.328	0.10	25.00	13.10	12.88 ± 0.04	11.87 ± 0.05	11.52 ± 0.06	0.84	1.00	E/S0	—
24	J044734.77+452912.6	71.895	45.487	159.885	0.237	0.41	50.35	8.87	13.14 ± 0.02	12.05 ± 0.02	11.56 ± 0.02	1.19	1.06	E/S0	—
25	J045332.55+453232.6	73.386	45.542	160.510	1.076	0.39	-23.08	14.16	13.09 ± 0.02	12.03 ± 0.02	11.56 ± 0.02	0.98	1.11	E/S0	—
26	J044639.43+454052.2	71.664	45.681	159.633	0.240	0.41	85.72	12.30	13.12 ± 0.02	12.08 ± 0.02	11.57 ± 0.02	1.25	1.01	E/S0	—
27	J044730.43+454548.7	71.877	45.764	159.666	0.406	0.20	47.01	10.49	13.14 ± 0.02	12.11 ± 0.02	11.62 ± 0.02	1.25	0.98	eS	—
28	J044953.41+451613.5	72.473	45.270	160.312	0.408	0.60	-60.00	15.10	13.33 ± 0.05	12.16 ± 0.04	11.71 ± 0.06	1.01	1.18	eS	—
29	J045032.79+445411.7	72.637	44.903	160.668	0.262	0.29	-10.36	12.04	13.26 ± 0.02	12.21 ± 0.02	11.71 ± 0.02	0.92	1.15	eS	—
30	J044940.04+451119.0	72.417	45.189	160.350	0.325	0.62	-10.81	13.76	13.23 ± 0.02	12.22 ± 0.02	11.72 ± 0.02	0.98	1.09	eS	—

Notes. The columns are: (1) the galaxy identifying number; (2) unique identifiers based on the right ascension (RA) and declination (Dec) ZoAJhhmss.ss±ddmss.s.; (3) & (4) equatorial coordinates, RA and Dec (J2000), respectively in degrees; (5) and (6) galactic longitude and latitude in degrees; (7) ellipticity in the K -band at the 20 mag arcsec⁻² isophote; (8) the K -band position angle in degrees, measured from celestial north to east; (9) the K_{20} isophotal major-axis radius in arcseconds; (10), (11) and (12) J , H and K band fiducial isophotal magnitudes (not corrected for foreground extinction); (13) the line-of-sight Galactic reddening in magnitudes; (14) $J^0 - K^0$ colours, corrected for foreground extinction; (15) the estimated morphology of galaxies; (16) the radial velocities from the WSRT HI measurements, and two optical velocities for the radio galaxies 3C 129 and 3C 129.1. v_{opt} : [*] Spinrad 1975, [x] Spinrad 1975, [+] $v_{opt} = 5150$ (Takata et al. 1994).

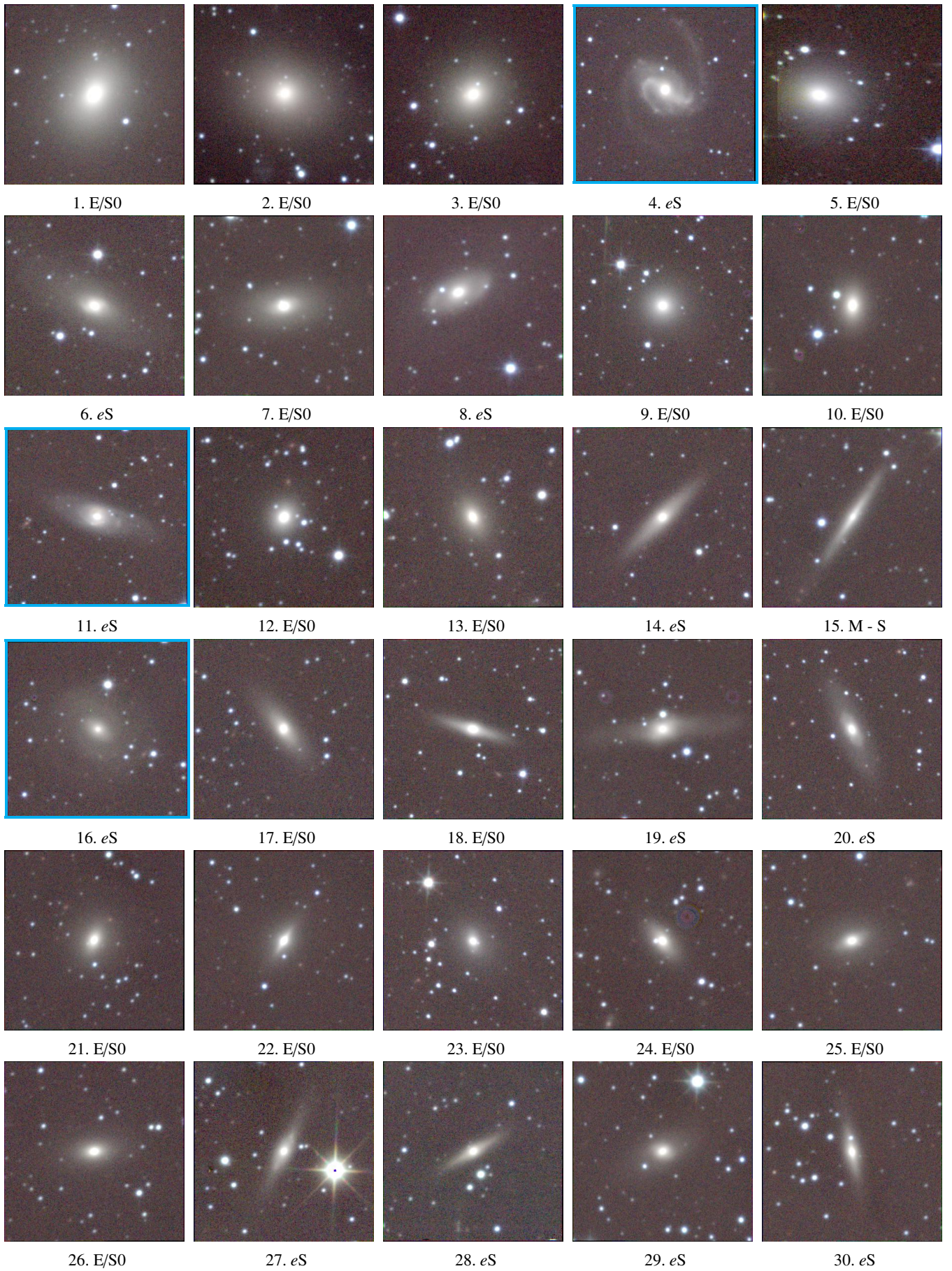


Fig. 9: The false-colour – J (blue), H (green) and K (red) representation ($1.2' \times 1.2'$) of the 30 brightest galaxy candidates in the 3C 129 cluster. The cyan frames indicate H I detection in the WSRT H I-survey.

3.2.2. Catalogue completeness

Given the severity and unknown small-scale patchiness of the Galactic extinction and the high stellar density in this Galactic field, it is non-trivial to perform a robust and quantitative completeness analysis. This type of analysis would involve measuring the detectability of model galaxies (as a function of magnitudes) which imitate the spatial surface brightness distribution of real galaxies. Since it is not possible to conduct such a quantitative completeness analysis in this ZoA region we estimate the completeness of the selected sample of the 3C129 cluster members using the technique described in Garilli et al. (1999) and Skelton et al. (2009). With this technique galaxies are not detectable when their central surface brightness falls below the detection limit at a given magnitude. Figure 10 shows the relation between the fiducial K -band aperture magnitudes and the central surface brightness of all galaxies (grey points) on the red sequence within the cluster radius. We performed a linear fit through these data points. This fit is shown by the black solid line (a) with the 1σ and -1σ deviation indicated by the dotted lines. The surface brightness limit of this sample is illustrated by the vertical grey dashed line (b). If we take the intercept of line a and b to be the completeness limit, then galaxies to the right of the line b and below line a are not detected (That is, this is completeness limit in K -band magnitude, based on the faintest surface brightness that is detected). However, there is a scatter in the distribution around the fitted line a , thus the completeness limit is at a magnitude where the line b intersects the -1σ line. Using this technique we derive a completeness limit of $K = 17.5$ mag for all 3C 129 galaxies on the red sequence.

However, for this study we only considered galaxies with $r_{K_{20}} > 3''$ (red points) as cluster members (see Sect. 3.1), this resulted in a change in the surface brightness limit but only modest changes in the linear fit and its scatter. Therefore, for the sample of galaxies on the red-sequence that we formally define as 3C 129 cluster members, we estimate a magnitude complete limit of $K = 15.6$ mag (or extinction corrected $K^o = 15.0$ mag).

To test the validity of our completeness estimates we use the cumulative galaxy counts shown in the bottom panel of Fig. 11 to derive the completeness limit. Since a linear increase is expected in these counts as a function of the K -band magnitude (for example, Kochanek et al. 2001) a deviation from this trend indicates incompleteness. Therefore, using this method the completeness magnitude of the 3C 129 galaxy sample is defined where the cumulative galaxy distribution flattens. By this technique we find that the $\log N$ distribution flattens at similar magnitudes as those derived from Fig. 10, that is., $\sim K = 15.6$ mag or extinction corrected $\sim K^o = 15.0$ mag. This also corresponds with the magnitude where the number counts start to decrease significantly as a function of the magnitude as shown in the histogram (bottom panel). Moreover, based on our visual inspection of the UKIDSS-GPS images, we are confident that we have identified all galaxies brighter than $K \approx 15.6$ mag ($K^o = 15.0$ mag). We refer to Table B and Fig. B (Appendix B) for a visual impression of galaxies with these magnitudes.

3.2.3. The 3C 129 cluster galaxy density

In this subsection we assess the density properties of the 3C 129 cluster. We conduct this by comparing the K -band magnitude distribution of its galaxies with those of three well-known galaxy clusters at similar distances. Our comparison sample comprises the Perseus, Coma and Norma galaxy clusters. All three repre-

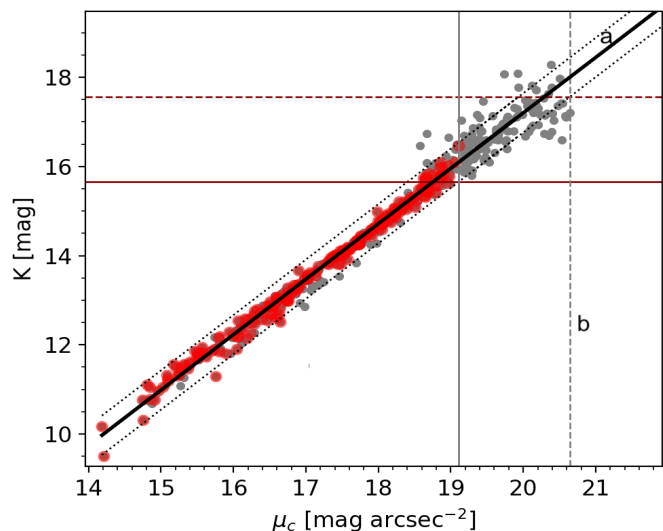


Fig. 10: An estimation of the galaxy magnitude completeness limit. The grey points are all galaxies on red sequence in the cluster radius. Red points are those with $r_{K_{20}} > 3''$ (that is, the cluster sample). Line a is the relation fitted through the grey points with the 1σ and -1σ deviation shown by the grey dotted lines. The surface brightness threshold for all 3C 129 galaxies on the red sequence is illustrated by line b . The completeness limit is given by the intercept of line b and the -1σ line. The corresponding surface brightness threshold and completeness limit lines for the bonafide cluster sample with $r_{K_{20}} > 3''$ are denoted by the solid grey vertical and red line, respectively.

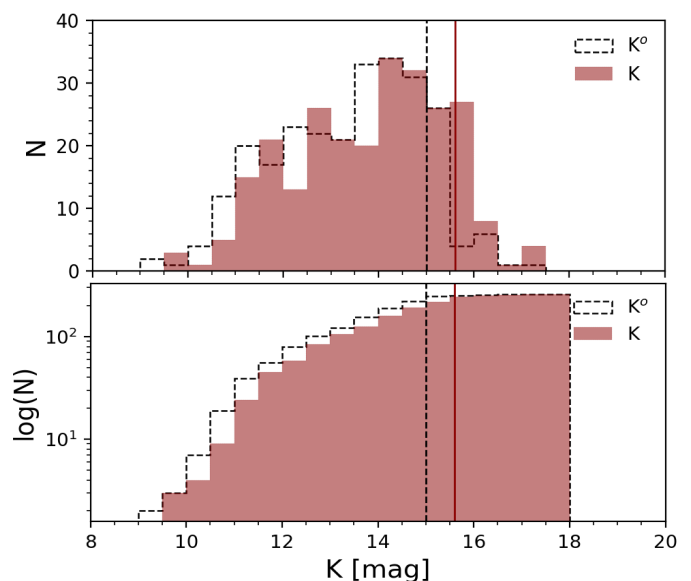


Fig. 11: The top panel is the histogram of the fiducial isophotal magnitudes for the K -band plotted in 0.5 magnitude bins and the bottom panel is the cumulative galaxy number count distribution as a function of the K -band magnitudes. In both panels the solid and dashed distributions represents the observed and extinction-corrected magnitudes, respectively. The estimated completeness magnitude limit is shown by the red vertical line for the observed magnitudes and dashed vertical line for the extinction corrected magnitudes.

sent well-studied and rich clusters nearby ($z \approx 0.02$). Parameters of these clusters are summarised in Table 2.

Table 2: A summary of parameters of comparison galaxy clusters.

Cluster	Distance Mpc	Cluster members catalogue
(1)	(2)	(3)
3C 129	89.1	This work
Perseus	76.6	Brunzendorf & Meusinger 1999
Norma	70.0	Skelton et al. 2009
Coma	98.9	Eisenhardt et al. 2007

The comparison samples for Perseus, Coma and Norma were selected from catalogues of confirmed galaxy cluster members by Brunzendorf & Meusinger (1999), Eisenhardt et al. (2007) and Skelton et al. (2009), respectively. We used 2MASX to extract the K -band elliptical aperture magnitudes of their galaxies at the 20 mag arcsec⁻² isophote by cross-correlating their positions with 2MASX sources. We only considered galaxies as matched if they were separated by less than 1.5'' in both catalogues. This offset corresponds to the maximum positional uncertainty between 2MASX and other galaxy catalogues (Kraan-Korteweg & Jarrett 2005).

Figure 12 shows the extinction corrected K -band magnitude distribution spanning the magnitude range $-16.5 \geq M_{K^0} \geq -26$ mag of the three clusters compared with the 3C 129 cluster. The galaxy number counts were only compared within the cores of the clusters over an area of radius, $r_{cl} = 0.5$ Mpc. The size of this area was chosen based on the confirmed galaxy members' sample with the smallest area coverage. The Coma distribution shows a steep increase in the galaxy counts from the bright end, $M_{K^0} \geq -26$ mag until it flattens at $M_{K^0} \geq -20.5$ mag reaching its maximum number counts. It only shows a slight downturn just before $M_{K^0} \approx -20$ mag because of the incompleteness of 2MASX at this magnitude. The Norma distribution shows a steady increase from the bright end with a downturn at $\sim M_{K^0} \approx -22$ mag, before the 2MASX completeness limit, while the Perseus distribution on the other hand does not show this number density and increase as seen in the Coma and Norma clusters. We find that compared to these three distributions, the 3C 129 cluster, shows the same number density on bright side and similar increase towards the faint end as the Perseus cluster. Based on this analysis we deduce that within the magnitude regime of, $-21.5 \leq M_{K^0} \leq -26.0$ mag (limited by 2MASX completeness), the central galaxy density within $r_{cl} = 0.5$ Mpc in the Coma and Norma cluster are comparable, while the 3C 129 cluster appears to be poorer than the aforementioned, but similar to the Perseus cluster.

4. The spatial distribution of the 3C 129 cluster galaxies

The spatial distribution of all galaxies on our defined red-sequence is shown in Fig. 13. The plot highlights the different morphologies and sizes of these galaxies. Members of the 3C 129 cluster are enclosed within the large dashed circle of radius of 1.7 Mpc centred on its X-ray emission ($\ell, b \approx 160.52^\circ, 0.27^\circ$). The smaller dotted circle encloses a prominent substructure to be discussed in Sect. 4.1. In this section we only discuss galaxies within the defined extent of the cluster (dashed circle).

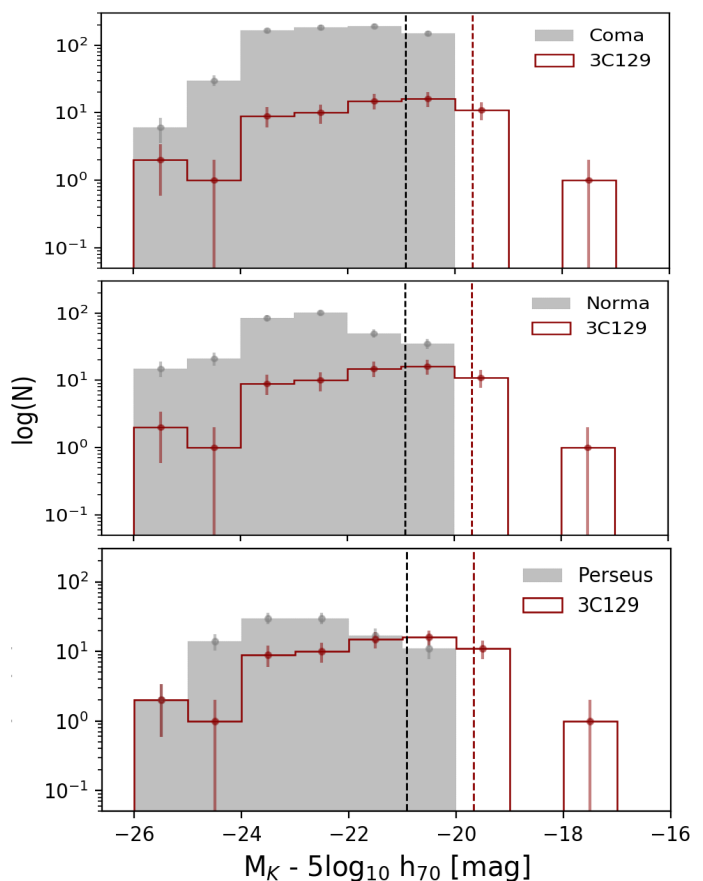


Fig. 12: Comparison of the extinction corrected K -band magnitude distribution (with Poisson error bars) per 1.0 mag bin of the 3C 129 cluster (red) with three well known clusters at similar distances, the Coma and Norma and Perseus clusters indicated by the solid histograms. The solid black and red lines are the respective 2MASX and 3C 129 UKIDSS sample completeness limits.

Galaxies within the inner region of the cluster of $r_{core} = 0.8$ Mpc, corresponding to its R_{500} (Piffaretti et al. 2011), are highly concentrated in the centre and are mostly early-type galaxies (E/S0). At larger projected radii the number of spirals (eS to Irr) increases steadily while the number of E/S0 galaxies decreases.

The spatial distribution in Fig. 13 is essentially a demonstration of the classical morphology-density relation (Dressler 1980). Most studies of the morphology-density (T - Σ) or morphology-radius (T - R) relation in galaxy clusters often use a composite of a large number of clusters to obtain an adequately high number of galaxies for each morphological type (Dressler 1980, Goto et al. 2003, Thomas & Katgert 2006). However, these composite (T - Σ) or (T - R) relations often lose information on the individual clusters. They also introduce large uncertainties given the large and sometimes inhomogeneous samples of clusters at different redshifts that are combined to make one cluster (Andreon 1996, van Dokkum et al. 2000).

To study the (T - R) relation specific to the 3C 129 cluster, we use a sample of all our classified galaxies (N=261). We show the results in Fig. 14 where the azimuthally averaged fractions of the morphological types are plotted as function of the projected distance from the core of the cluster to the outskirts. The fraction of E/S0 galaxies decreases from $\sim 36\%$ in the core to almost 22%

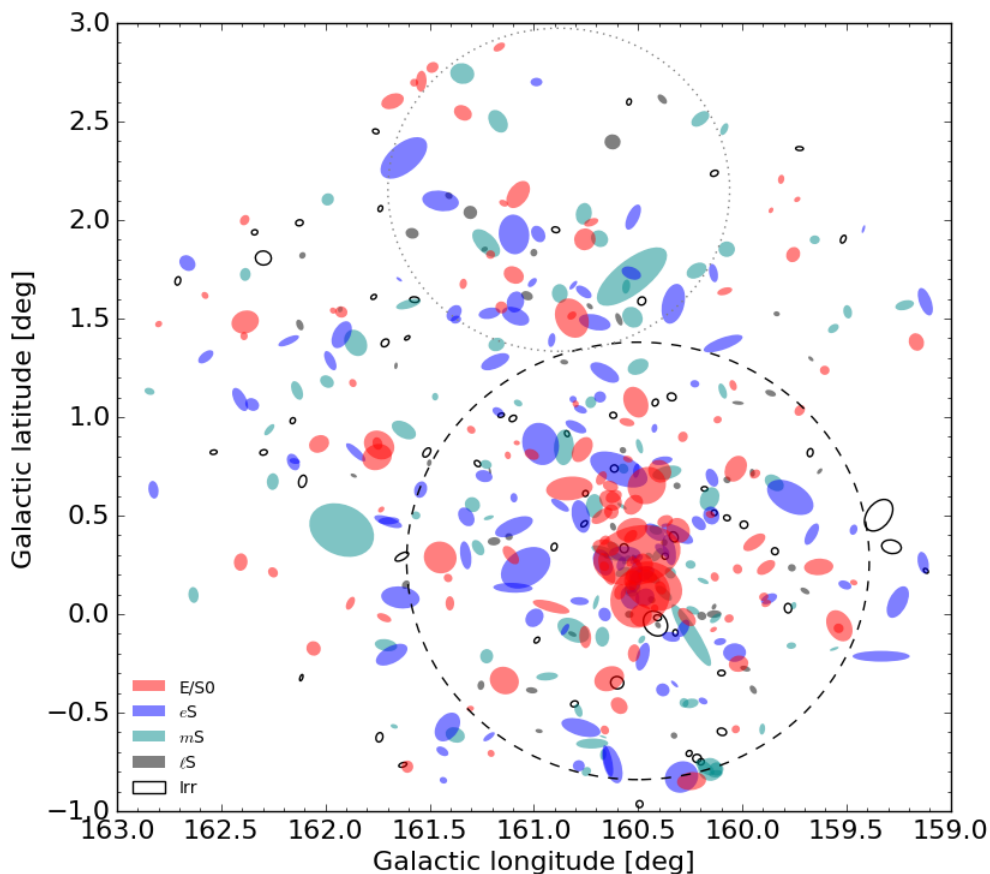


Fig. 13: Spatial distribution of galaxies on the red sequence. Points sizes and shapes are shown relative to their radii, ellipticities and positions angles. The defined projected radius of the cluster, $r_{cl} = 1.7$ Mpc is shown by the black dashed line. The substructure of the cluster as described in Sect. 4.1 is denoted by the smaller dotted grey circle. The different colours illustrate the morphologies of the galaxies.

in the outskirts of the cluster. The early spirals (eS) fraction increases from 24% and peaks to 29% where the E/S0 population is lowest at $r_{cl} = 1.1$ Mpc and then decreases rapidly to 22% similar to the E/S0 fraction. On the other hand, lS and Irr galaxies show the opposite trend with an increasing fraction from the core towards the cluster outskirts. The morphology-radius relation of the 3C 129 cluster shows an obvious morphological segregation that is qualitatively consistent with those of the centrally concentrated rich clusters (Dressler et al. 1997).

4.1. Substructure in the 3C 129 cluster

4.1.1. Projected density distribution

To investigate the possible presence of substructure we analyse the projected galaxy number densities which is apparent already in Fig. 13. Although this method ignores the redshift information it is optimal at identifying substructures with enhanced densities that are relatively large in separation (Pinkney et al. 1996). For the galaxies on the red sequence we study the projected galaxy number density using the bivariate kernel density estimator (Feigelson & Babu 2012),

$$f_{kern}(\mathbf{x}, \mathbf{h}) = \frac{1}{n \prod_{j=1}^p h_j} \sum_{i=1}^n \left[\prod_{j=1}^p h_j G_k \left(\frac{\mathbf{x}_i - \mathbf{x}_{ij}}{h_{ij}} \right) \right] \quad (6)$$

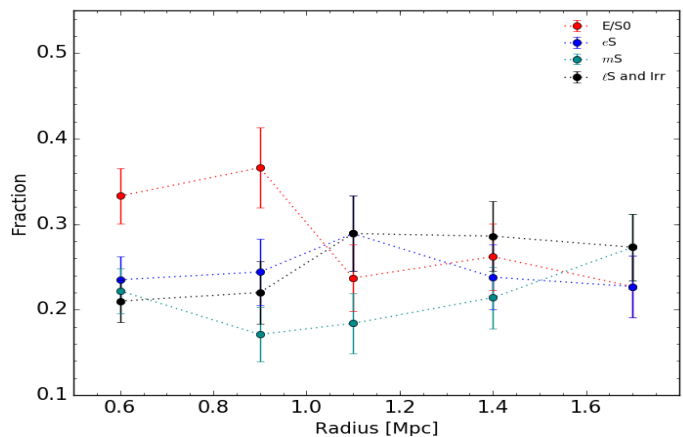


Fig. 14: The morphology-radius relation for the E/S0 (red), eS (blue), mS (darkcyan), lS & Irr (black) members of the cluster.

where $p = 2$ is the number of variables, which are Galactic coordinates (ℓ, b) in our case represented by $\mathbf{X}_i = \mathbf{X}_{i1}, \mathbf{X}_{i2}$, with the smoothing length (bandwidth), $\mathbf{h} = (h_1, h_2)$. The number of galaxies is denoted by n and the bivariate Gaussian kernel function by G_k .

The resulting density map constructed with the red sequence galaxies is plotted in Fig. 15. It shows a distribution that is slightly elongated north-east to south-west in Galactic coordi-

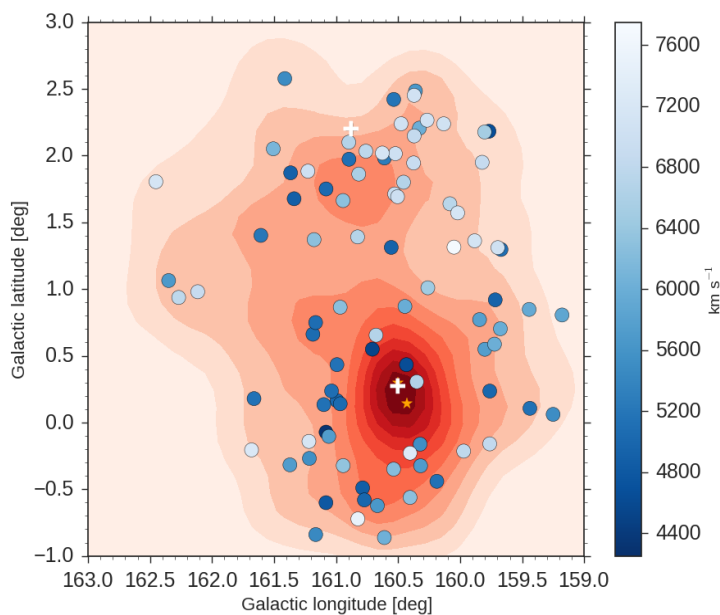


Fig. 15: A two-dimensional kernel density map of galaxies on the red-sequence (red) in position space. Dots in gradient blues are galaxies detected in HI over the radial velocity range of the 3C 129 cluster ($4000 - 8000 \text{ km s}^{-1}$). The displayed colour bar is the velocity range of the HI galaxies. The two white plus markers indicate the position of the X-ray emission over which the cluster is centred and the location near which the 3C129-A group lies and the orange stars are positions of the two radio sources, 3C129 and 3C129.1.

nates. This is possibly related to an intrinsically more elongated mass distribution of the large-scale filamentary structure (PPS) within which this cluster is embedded. Upon closer inspection two distinct structures become apparent. A dominant density peak corresponds to the 3C 129 cluster centre, located at $(\ell, b) \approx (160.52^\circ, 0.27^\circ)$. The other, a more diffuse density peak about 2.9 Mpc (assuming $z = 0.02$) north from the cluster core located near $(\ell, b) \approx (160.88^\circ, 2.20^\circ)$, indicates a substructure, henceforth called the 3C129-A group.

A comparison with the X-ray emission map in Fig. 1 reveals that the core of the cluster is closely aligned with the X-ray gas emission. The X-ray contours are irregular and are not associated with any X-ray point source in the cluster. Thus supporting what was inferred by Leahy & Yin (2000) that the 3C 129 cluster is under assembly through a merger and it is possibly growing along the filament.

Furthermore, we compared this galaxy projected density distribution with the spatial distribution of galaxies detected in HI in the velocity range of the cluster, marked by gradient blue dots. The latter shows the 3C129-A group to be more populated by HI-rich galaxies and also shows galaxies to have distinctly higher velocities than those around the core of the 3C 129 cluster. Furthermore, a relatively smaller number of HI detections was found in the core of the cluster, which is indicative of a gas removal mechanism taking place in this region. The implication of this is beyond the scope of this paper and will be discussed in detail in a paper that follows where we will be analysing the environmental effects on the HI properties of the galaxies.

4.1.2. Velocity distribution

Having established the existence of the projected 3C129-A substructure in association with the 3C 129 cluster, we now investigate the radial velocity distribution of their constituent galaxies. We do this by using the 87 galaxies with measured HI radial velocities within the velocity range of the cluster's parent supercluster (PPS) of $4000 - 8000 \text{ km s}^{-1}$ with and without a NIR-counterpart (Ramatsoku et al. 2016). A visual inspection of Fig. 16 indicates a bimodal velocity distribution of the HI detections. To check whether the velocity distribution is indeed statistically different from a Gaussian distribution we applied a Lilliefors test (see Feigelson & Babu 2012). The resulting p -value is $p < 0.01$ which indicates that the null hypothesis, which states that the full distribution is Gaussian, can be rejected, thus consistent with the presence of substructure in the radial velocity distribution.

We estimate the mean radial velocities of the two structures by selecting 43 HI-detected galaxies within a radius of 1.1° centred on the cluster's centre, and 44 within a radius of 0.8° centred on the 3C129-A group (see Fig. 13). The latter's radius was chosen to be as large as possible while maintaining mutual exclusivity with the 3C 129 cluster. The velocity distributions of the galaxies selected in the two structures are shown in Fig. 16. We fit two Gaussian profiles and obtained $cz = 5227 \pm 171 \text{ km s}^{-1}$ and $\sigma = 1097 \pm 252 \text{ km s}^{-1}$ for the 3C 129 cluster and $cz = 6923 \pm 71 \text{ km s}^{-1}$ and $\sigma = 422 \pm 100 \text{ km s}^{-1}$ for the 3C129-A group. We note that the velocity dispersion of the cluster is higher than that which was determined from the β -model of the cluster of $\sigma = 765 \text{ km s}^{-1}$ (Leahy & Yin 2000) but also note that our measurement is subject to large uncertainties given the lack of optical spectroscopy for gas-poor galaxies in the cluster core.

Combining the results from the velocity and density distribution analysis we find a distinct substructure to the north of the 3C 129 cluster with higher velocity and more gas-rich spirals. Although the line-of-sight velocity difference of $cz_{gr} - cz_{cl} = 1696 \pm 185 \text{ km s}^{-1}$ is quite large, it is possible that the 3C129-A group is falling into the cluster. In paper III we will also perform a Tully-Fisher analysis to get hints of the infall properties of the group. A more detailed and robust dynamical analysis can only be conducted with more redshifts of the gas-poor galaxies in the cluster and the immediate surrounding regions.

5. Summary

We combined near-infrared images and colours from the UKIDSS Galactic Plane Survey with HI data from the Westerbork Synthesis Radio Telescope, in and around the 3C 129 cluster to identify its galaxy members. This was done by analysing the properties of the $J - K$ versus K magnitude of galaxies to define and fit the red-sequence of this cluster. The slope of its red sequence was found to be $\alpha = -0.023 \pm 0.002 \text{ mag}$, similar to the Coma cluster ($\alpha = -0.017 \pm 0.009$). We determined the extent of the cluster, centred on the X-ray emission, out to a radius of 1.7 Mpc ($1.34R_{200}$), and obtained a sample of 261 identified 3C 129 cluster galaxies with $r_{K_{20}} > 3''$. Of these, 26 have redshift measurements, 24 from our WSRT HI observations and 3 from previous optical observations. A catalogue and colour images of the galaxy cluster members is presented with the photometric parameters. We note that the way the catalogue was defined and the lack of redshifts might lead to contamination of $\leq 5\%$ by background galaxies.

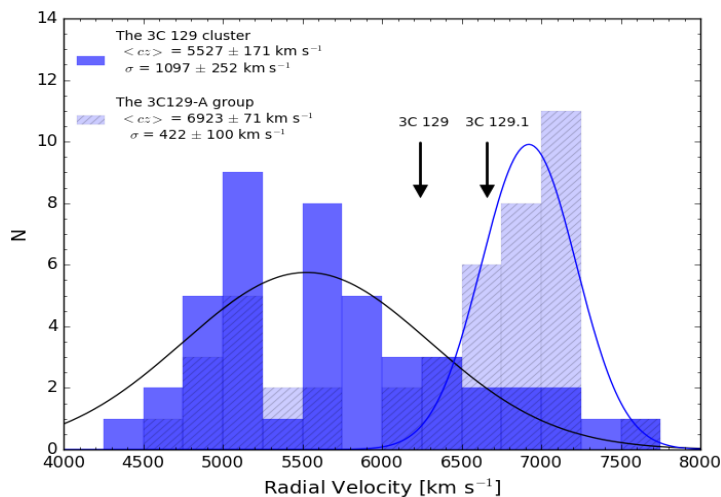


Fig. 16: The distribution of radial velocities of the 3C 129 cluster (dark blue) and its northern substructure; 3C 129-A (hatched light blue). Velocities bins are 250 km s^{-1} wide. The black line is a fitted Gaussian profile of the 3C 129 cluster and blue line for the 3C 129-A group. The radial velocities of the radio sources, 3C 129 and 3C 129.1 are indicated by arrows.

The galaxies within the core radius of the 3C 129 cluster were used to assess its galaxy density, which we compared with those of three well-known clusters at similar redshift, namely the Coma, Norma and Perseus clusters. Results show that the galaxy density at the core of the 3C 129 cluster is lower than in the Coma and Norma cluster, but comparable to that in the Perseus. This places the 3C 129 cluster among the richest clusters in the Perseus-Pisces filament.

We visually determined the approximate morphologies of all the 261 cluster galaxies using UKIDSS images and derived the morphology-radius relation of the cluster. A clear morphological segregation occurs at 0.6 - 0.9 Mpc from the cluster core, where the fraction of early-type galaxies increases inwards to more than 35%, while the fraction of late-type galaxies drops to about 16%. The segregation continues towards the cluster outskirts where the fraction of early-type galaxies drops to 22% and the fraction of late-types increases to almost 30%. In paper III we will assess how the environment may have affected the morphologies of these galaxies.

The peak of the spatial distribution of the galaxies in the 3C 129 cluster core shows no HI detections implying a HI deficient cluster centre, consistent with rich cluster environments. The core galaxy distribution also shows a slight asymmetry which is aligned with the irregular X-ray emission and not associated with any X-ray point source or any galaxy in the cluster. These features strengthen claims by Leahy & Yin (2000) that the cluster has undergone (or is undergoing) a merger and has not yet reached a dynamically relaxed state. The HI-detected galaxies around the cluster core were measured to have, $cz = 5227 \pm 171 \text{ km s}^{-1}$ with $\sigma = 1097 \pm 252 \text{ km s}^{-1}$. We identified a substructure to the north of the main central region with a radial velocity distribution of $cz = 6923 \pm 71 \text{ km s}^{-1}$ and $\sigma = 422 \pm 100 \text{ km s}^{-1}$. We suspect that this substructure is infalling, which suggests the cluster is still growing by accreting from its parent large-scale structure that forms the Perseus-Pisces filament. However, this remains unconfirmed as

more detailed analyses are required. These will be performed as part of the analysis of the 3C 129 cluster in paper III.

Acknowledgements. The authors would like to thank Hans Boehringer and Gaying Chon for assisting with the X-ray data reduction for this study. We thank the anonymous reviewer for the helpful comments and suggestions. MR acknowledges financial support from the Ubbo Emmius Fund of the University of Groningen and the financial support provided by SKA South-Africa and the South African National Research Foundation. The SA and NL authors of this collaboration all benefitted tremendously from collaborative exchanges support by the NRF/NWO bilateral agreement for Astronomy and Astronomy Enabling Technologies. MR's research is supported by the SARAO HCD programme via the "New Scientific Frontiers with Precision Radio Interferometry" research group grant. This work is based upon research supported by the South African Research Chairs Initiative of the Department of Science and Technology and National Research Foundation. MR also acknowledges INAF-OAC for their support. We would also like to thank W. Williams for the photometric contributions to the project. This research has also made use of the UKIRT Infrared Deep Sky Survey database. We acknowledge the UKIDSS support team, including M. Reads, S Hodgkin and P. Lucas for their various support on assessing the UKIDSS images. This work is part of MV's Vici research programme "The Panoramic Perspective on Gas and Galaxy Evolution" with project number 016.130.338, and (partly) financed by the Netherlands Organisation for Scientific Research (NWO).

References

- Allen, S. W., Schmidt, R. W., Ebeling, H., Fabian, A. C., & van Speybroeck, L. 2004, *MNRAS*, 353, 457
- Andreon, S. 1996, *A&A*, 314, 763
- Bell, E. F., Wolf, C., Meisenheimer, K., et al. 2004, *ApJ*, 608, 752
- Bertin, E. & Arnouts, S. 1996, *A&AS*, 117, 393
- Borgani, S., Rosati, P., Tozzi, P., et al. 2001, *ApJ*, 561, 13
- Bower, R. G., Lucey, J. R., & Ellis, R. S. 1992, *MNRAS*, 254, 589
- Brunzendorf, J. & Meusinger, H. 1999, *A&AS*, 139, 141
- Buta, R. J. & McCall, M. L. 1999, *ApJS*, 124, 33
- Cassata, P., Cimatti, A., Kurk, J., et al. 2008, *A&A*, 483, L39
- Chilingarian, I. V., Melchior, A.-L., & Zolotukhin, I. Y. 2010, *MNRAS*, 405, 1409
- Chung, A., van Gorkom, J. H., Kenney, J. D. P., Crowl, H., & Vollmer, B. 2009, *AJ*, 138, 1741
- Cirasuolo, M., McLure, R. J., Dunlop, J. S., et al. 2007, *MNRAS*, 380, 585
- Cohen, M., Wheaton, W. A., & Megeath, S. T. 2003, *AJ*, 126, 1090
- Condon, J. J., Cotton, W. D., Greisen, E. W., et al. 1998, *AJ*, 115, 1693
- Conselice, C. J., Gallagher, III, J. S., & Wyse, R. F. G. 2003, *AJ*, 125, 66
- Dressler, A. 1980, *ApJ*, 236, 351
- Dressler, A., Oemler, Jr., A., Couch, W. J., et al. 1997, *ApJ*, 490, 577
- Drinkwater, M. J., Gregg, M. D., & Colless, M. 2001, *ApJ*, 548, L139
- Dye, S., Warren, S. J., Hambly, N. C., et al. 2006, *MNRAS*, 372, 1227
- Ebeling, H., Edge, A. C., Bohringer, H., et al. 1998, *MNRAS*, 301, 881
- Ebeling, H., Mullis, C. R., & Tully, R. B. 2002, *ApJ*, 580, 774
- Eisenhardt, P. R., De Propris, R., Gonzalez, A. H., et al. 2007, *ApJS*, 169, 225
- Feigelson, E. D. & Babu, G. J. 2012, *Modern Statistical Methods for Astronomy*
- Fitzpatrick, E. L. 1999, *PASP*, 111, 63
- Forman, W., Jones, C., Cominsky, L., et al. 1978, *ApJS*, 38, 357
- Franzetti, P., Scodreggio, M., Garilli, B., et al. 2007, *A&A*, 465, 711
- Garilli, B., Maccagni, D., & Andreon, S. 1999, *A&A*, 342, 408
- Giovanelli, R. & Haynes, M. P. 1985, *AJ*, 90, 2445
- Gladders, M. D., López-Cruz, O., Yee, H. K. C., & Kodama, T. 1998, *ApJ*, 501, 571
- Gladders, M. D. & Yee, H. K. C. 2000, *AJ*, 120, 2148
- Goto, T., Yamauchi, C., Fujita, Y., et al. 2003, *MNRAS*, 346, 601
- Hammer, D., Verdoes Kleijn, G., Hoyos, C., et al. 2010, *ApJS*, 191, 143
- Hanski, M. O., Theureau, G., Ekholm, T., & Teerikorpi, P. 2001, *A&A*, 378, 345
- Harris, D. E., Krawczynski, H., & Taylor, G. B. 2002, *ApJ*, 578, 60
- Haynes, M. P. & Giovanelli, R. 1986, *ApJ*, 306, L55
- Haynes, M. P., Magri, C., Giovanelli, R., & Starosta, B. M. 1988, *AJ*, 95, 607
- Henning, P. A., Springob, C. M., Minchin, R. F., et al. 2010, *AJ*, 139, 2130
- Hodgkin, S. T., Irwin, M. J., Hewett, P. C., & Warren, S. J. 2009, *MNRAS*, 394, 675
- Hudson, M. J., Lucey, J. R., Smith, R. J., & Steel, J. 1997, *MNRAS*, 291, 488
- Hughes, J. P. 1989, *ApJ*, 337, 21
- Jaegers, W. J. & de Grijs, M. H. K. 1983, *A&A*, 127, 235
- Jarrett, T. 2004, *PASA*, 21, 396
- Jarrett, T.-H., Chester, T., Cutri, R., et al. 2000, *AJ*, 120, 298

- Karachentsev, I. D., Tully, R. B., Wu, P.-F., Shaya, E. J., & Dolphin, A. E. 2014, *ApJ*, 782, 4
- Kochanek, C. S., Pahre, M. A., Falco, E. E., et al. 2001, *ApJ*, 560, 566
- Kraan-Korteweg, R. C. & Jarrett, T. 2005, *Astronomical Society of the Pacific Conference Series*, Vol. 329, *The Zone of Avoidance: Optical Compared to Near-Infrared Searches*, ed. A. P. Fairall & P. A. Woudt, 119
- Kraan-Korteweg, R. C. & Lahav, O. 2000, *A&A Rev.*, 10, 211
- Kraan-Korteweg, R. C., Loan, A. J., Burton, W. B., et al. 1994, *Nature*, 372, 77
- Kraan-Korteweg, R. C., van Driel, W., Schröder, A. C., Ramatsoku, M., & Henning, P. A. 2018, *MNRAS*, 481, 1262
- Krawczynski, H., Harris, D. E., Grossman, R., et al. 2003, *MNRAS*, 345, 1255
- Lal, D. V. & Rao, A. P. 2004, *A&A*, 420, 491
- Lawrence, A., Warren, S. J., Almaini, O., et al. 2007, *MNRAS*, 379, 1599
- Leahy, D. A. & Yin, D. 2000, *MNRAS*, 313, 617
- López-Cruz, O., Barkhouse, W. A., & Yee, H. K. C. 2004, *ApJ*, 614, 679
- Lucas, P. W., Hoare, M. G., Longmore, A., et al. 2008, *MNRAS*, 391, 136
- Mantz, A., Allen, S. W., Rapetti, D., & Ebeling, H. 2010, *MNRAS*, 406, 1759
- Masters, K. L., Springob, C. M., & Huchra, J. P. 2008, *AJ*, 135, 1738
- McIntyre, T. P., Henning, P. A., Minchin, R. F., Momjian, E., & Butcher, Z. 2015, *AJ*, 150, 28
- Mei, S., Holden, B. P., Blakeslee, J. P., et al. 2009, *ApJ*, 690, 42
- Menci, N., Fontana, A., Giallongo, E., & Salimbeni, S. 2005, *ApJ*, 632, 49
- Miller, N. A., Hornschemeier, A. E., Mobasher, B., et al. 2009, *AJ*, 137, 4450
- Muldrew, S. I., Hatch, N. A., & Cooke, E. A. 2015, *MNRAS*, 452, 2528
- Murgia, M., Govoni, F., Carretti, E., et al. 2016, *MNRAS*, 461, 3516
- Mutabazi, T., Blyth, S. L., Woudt, P. A., et al. 2014, *MNRAS*, 439, 3666
- Ouchi, M., Shimasaku, K., Akiyama, M., et al. 2005, *ApJ*, 620, L1
- Owen, F. N., Burns, J. O., Rudnick, L., & Greisen, E. W. 1979, *ApJ*, 229, L59
- Piffaretti, R., Arnaud, M., Pratt, G. W., Pointecouteau, E., & Melin, J.-B. 2011, *A&A*, 534, A109
- Pinkney, J., Roettiger, K., Burns, J. O., & Bird, C. M. 1996, *ApJS*, 104, 1
- Ramatsoku, M., Kraan-Korteweg, R., Schröder, A., & van Driel, W. 2014, *ArXiv e-prints* [arXiv:1412.5324]
- Ramatsoku, M., Verheijen, M. A. W., Kraan-Korteweg, R. C., et al. 2016, *MNRAS*, 460, 923
- Riad, I. F., Kraan-Korteweg, R. C., & Woudt, P. A. 2010, *MNRAS*, 401, 924
- Roman, A. T., Iwata, I., & Saitō, M. 2000, *ApJS*, 127, 27
- Sanchez-Barrantes, M., Henning, P. A., McIntyre, T., et al. 2019, *AJ*, 158, 234
- Scarlata, C., Carollo, C. M., Lilly, S., et al. 2007, *ApJS*, 172, 406
- Schlafly, E. F. & Finkbeiner, D. P. 2011, *ApJ*, 737, 103
- Schlegel, D. J., Finkbeiner, D. P., & Davis, M. 1998, *ApJ*, 500, 525
- Skelton, R. E., Woudt, P. A., & Kraan-Korteweg, R. C. 2009, *MNRAS*, 396, 2367
- Spinrad, H. 1975, *ApJ*, 199, L1
- Spitler, L. R., Labbé, I., Glazebrook, K., et al. 2012, *ApJ*, 748, L21
- Springel, V., White, S. D. M., Jenkins, A., et al. 2005, *Nature*, 435, 629
- Staveley-Smith, L., Kraan-Korteweg, R. C., Schröder, A. C., et al. 2016, *AJ*, 151, 52
- Stetson, P. B. 1987, *PASP*, 99, 191
- Stott, J. P., Pimbblet, K. A., Edge, A. C., Smith, G. P., & Wardlow, J. L. 2009, *MNRAS*, 394, 2098
- Takata, T., Yamada, T., Saito, M., Chamaraux, P., & Kazes, I. 1994, *A&AS*, 104
- Tanaka, M., De Breuck, C., Venemans, B., & Kurk, J. 2010, *A&A*, 518, A18
- Taylor, E. N., Franx, M., van Dokkum, P. G., et al. 2009, *ApJ*, 694, 1171
- Taylor, G. B., Govoni, F., Allen, S. W., & Fabian, A. C. 2001, *MNRAS*, 326, 2
- Thomas, T. & Katgert, P. 2006, *A&A*, 446, 31
- Valentinuzzi, T., Poggianti, B. M., Fasano, G., et al. 2011, *A&A*, 536, A34
- van Dokkum, P. G., Franx, M., Fabricant, D., Illingworth, G. D., & Kelson, D. D. 2000, *ApJ*, 541, 95
- van Driel, W., Schneider, S. E., Kraan-Korteweg, R. C., & Monnier Ragaigine, D. 2009, *A&A*, 505, 29
- Vikhlinin, A., Kravtsov, A. V., Burenin, R. A., et al. 2009, *ApJ*, 692, 1060
- Visvanathan, N. & Sandage, A. 1977, *ApJ*, 216, 214
- Weinzirl, T., Jooe, S., Neistein, E., et al. 2014, *MNRAS*, 441, 3083
- White, R. L. & Becker, R. H. 1992, *ApJS*, 79, 331
- Woudt, P. A., Fairall, A., Kraan-Korteweg, R. C., et al. 2005, in *Astronomical Society of the Pacific Conference Series*, Vol. 329, *Nearby Large-Scale Structures and the Zone of Avoidance*, ed. A. P. Fairall & P. A. Woudt, Fairall

Appendix A: Source extractor parameters

Table A.1: Parameters for SEXTRACTOR 2.8.6.

Parameter	Value
DETECT_MINAREA	50 (10 for sources above 9σ)
DETECT_THRESH	3 (9 for min. of 50 adjacent pixels)
ANALYSIS_THRESH	3
FILTER	Y
FILTER_NAME	default.conv
DEBLEND_NTHRESH	32
DEBLEND_MINCONT	0.001
CLEAN	Y
CLEAN_PARAM	1.0
MASK_TYPE	CORRECT
PHOT_APERTURES	5
PHOT_AUTOPARAMS	2.5, 3.5
PHOT_PETROPARAMS	2.0, 3.5
SATUR_LEVEL	422784/ADU
MAG_ZEROPOINT	24.105
GAIN	4.5/e-/ADU
GAIN_KEY	GAIN
PIXEL_SCALE	0.4/arcsec
SEEING_FWHM	0.8/arcsec
STARNNW_NAME	default.nnw
BACK_SIZE	64
BACK_FILTERSIZE	3
BACKPHOTO_TYPE	GLOBAL

Appendix B: The near-infrared images

Table B. Near-infrared parameters of the 3C 129 candidate cluster galaxies.

ID no.	Unique ID	RA	Dec	ℓ	b	ϵ_K	ϕ_K	r_{K20}	J_{K20}	H_{K20}	K_{20}	$E(B-V)$	$J^\circ - K^\circ$	Type	v_{rad}
	ZoA	deg	deg	deg	deg		deg	"	mag	mag	mag	mag	mag		km s ⁻¹
(1)	(2)	(3)	(4)	(5)	(6)	(7)	(8)	(9)	(10)	(11)	(12)	(13)	(14)	(15)	(16)
1	J044908.26+445540.3	72.284	44.928	160.490	0.086	0.17	24.71	28.10	10.96 ± 0.02	9.94 ± 0.02	9.51 ± 0.02	0.89	1.07	E/S0	—
2	J045006.67+450305.8	72.528	45.052	160.505	0.298	0.20	65.00	37.30	11.21 ± 0.04	10.10 ± 0.04	9.59 ± 0.04	0.98	1.20	E/S0	6655*
3	J044909.06+450039.4	72.288	45.011	160.427	0.142	0.10	-60.00	25.60	11.50 ± 0.03	10.46 ± 0.04	10.00 ± 0.04	0.94	1.10	E/S0	6236 ^x
4	J045145.56+443602.6	72.940	44.601	161.039	0.235	0.40	60.00	22.80	11.75 ± 0.03	10.82 ± 0.03	10.35 ± 0.04	0.79	1.07	eS	5086 ⁺
5	J044939.78+440922.1	72.416	44.156	161.141	-0.337	0.09	-55.01	12.79	12.05 ± 0.02	11.16 ± 0.02	10.76 ± 0.02	0.65	1.01	E/S0	—
6	J044842.39+454818.5	72.177	45.805	159.769	0.593	0.40	-61.15	21.62	12.25 ± 0.02	11.23 ± 0.02	10.77 ± 0.02	1.12	1.00	eS	—
7	J045245.69+450106.2	73.190	45.018	160.829	0.638	0.44	85.11	19.63	12.31 ± 0.02	11.23 ± 0.02	10.78 ± 0.02	0.94	1.12	E/S0	—
8	J045219.88+451546.1	73.083	45.263	160.592	0.734	0.50	-60.00	25.90	12.23 ± 0.05	11.26 ± 0.05	10.83 ± 0.06	0.91	1.00	eS	—
9	J045326.75+441900.7	73.361	44.317	161.449	0.288	0.06	26.77	14.31	12.32 ± 0.02	11.38 ± 0.02	10.96 ± 0.02	0.69	1.06	E/S0	—
10	J045045.92+450659.7	72.691	45.117	160.529	0.428	0.27	0.36	13.39	12.62 ± 0.02	11.56 ± 0.02	11.05 ± 0.02	1.00	1.14	E/S0	—
11	J044719.31+441701.6	71.830	44.284	160.774	-0.576	0.47	-73.54	16.96	12.50 ± 0.02	11.56 ± 0.02	11.06 ± 0.02	0.69	1.15	eS	4993
12	J044843.25+445216.0	72.180	44.871	160.486	-0.007	0.11	32.33	9.98	12.54 ± 0.02	11.54 ± 0.02	11.11 ± 0.02	0.84	1.07	E/S0	—
13	J044459.45+453344.1	71.248	45.562	159.534	-0.059	0.30	-23.53	14.62	12.83 ± 0.02	11.73 ± 0.02	11.19 ± 0.02	1.35	1.06	E/S0	—
14	J044429.89+442914.8	71.125	44.487	160.291	-0.827	0.31	44.80	14.65	12.81 ± 0.02	11.78 ± 0.02	11.23 ± 0.02	0.98	1.16	eS	—
15	J044724.21+445928.3	71.851	44.991	160.244	-0.107	0.80	-35.00	31.50	12.64 ± 0.05	11.67 ± 0.05	11.25 ± 0.07	0.84	1.03	mS	—
16	J045414.90+450315.1	73.562	45.054	160.967	0.864	0.17	-41.28	19.00	12.79 ± 0.02	11.75 ± 0.02	11.29 ± 0.02	0.93	1.10	eS	6269
17	J045129.31+451852.0	72.872	45.314	160.458	0.652	0.57	-35.96	17.04	12.86 ± 0.02	11.84 ± 0.02	11.31 ± 0.02	1.04	1.10	E/S0	—
18	J045028.01+443407.6	72.617	44.569	160.916	0.037	0.70	-74.56	15.98	12.74 ± 0.02	11.79 ± 0.02	11.32 ± 0.02	0.80	1.07	E/S0	—
19	J045156.57+445815.0	72.986	44.971	160.774	0.496	0.47	-12.60	14.73	12.79 ± 0.02	11.79 ± 0.02	11.33 ± 0.02	0.94	1.05	eS	—
20	J045251.94+444122.5	73.216	44.690	161.095	0.443	0.56	63.37	16.94	12.90 ± 0.02	11.92 ± 0.02	11.47 ± 0.02	0.85	1.07	eS	—
21	J045018.46+454152.2	72.577	45.698	160.031	0.738	0.27	24.97	12.06	13.08 ± 0.02	11.99 ± 0.02	11.49 ± 0.02	1.17	1.08	E/S0	—
22	J045324.45+451127.6	73.352	45.191	160.768	0.835	0.40	29.03	12.08	12.97 ± 0.02	11.93 ± 0.02	11.50 ± 0.02	0.98	1.05	E/S0	—
23	J044753.50+443250.9	71.973	44.547	160.638	-0.328	0.10	25.00	13.10	12.88 ± 0.04	11.87 ± 0.05	11.52 ± 0.06	0.84	1.00	E/S0	—
24	J044734.77+452912.6	71.895	45.487	159.885	0.237	0.41	50.35	8.87	13.14 ± 0.02	12.05 ± 0.02	11.56 ± 0.02	1.19	1.06	E/S0	—
25	J045332.55+453232.6	73.386	45.542	160.510	1.076	0.39	-23.08	14.16	13.09 ± 0.02	12.03 ± 0.02	11.56 ± 0.02	0.98	1.11	E/S0	—
26	J044639.43+454052.2	71.664	45.681	159.633	0.240	0.41	85.72	12.30	13.12 ± 0.02	12.08 ± 0.02	11.57 ± 0.02	1.25	1.01	E/S0	—
27	J044730.43+454548.7	71.877	45.764	159.666	0.406	0.20	47.01	10.49	13.14 ± 0.02	12.11 ± 0.02	11.62 ± 0.02	1.25	0.98	eS	—
28	J044953.41+451613.5	72.473	45.270	160.312	0.408	0.60	-60.00	15.10	13.33 ± 0.05	12.16 ± 0.04	11.71 ± 0.06	1.01	1.18	eS	—
29	J045032.79+445411.7	72.637	44.903	160.668	0.262	0.29	-10.36	12.04	13.26 ± 0.02	12.21 ± 0.02	11.71 ± 0.02	0.92	1.15	eS	—
30	J044940.04+451119.0	72.417	45.189	160.350	0.325	0.62	-10.81	13.76	13.23 ± 0.02	12.22 ± 0.02	11.72 ± 0.02	0.98	1.09	eS	—
31	J045020.02+445348.1	72.583	44.897	160.649	0.229	0.58	-15.99	14.81	13.20 ± 0.02	12.22 ± 0.02	11.73 ± 0.02	0.95	1.06	E/S0	—
32	J045049.32+445742.3	72.706	44.962	160.655	0.337	0.36	-76.66	11.22	13.28 ± 0.02	12.26 ± 0.02	11.80 ± 0.02	0.91	1.09	E/S0	—
33	J045346.20+450747.8	73.443	45.130	160.855	0.846	0.41	7.89	15.79	13.31 ± 0.02	12.22 ± 0.02	11.80 ± 0.02	0.96	1.09	mS	—
34	J044414.05+443036.7	71.059	44.510	160.243	-0.848	0.39	28.13	12.21	13.30 ± 0.02	12.30 ± 0.02	11.81 ± 0.02	1.01	1.05	E/S0	—
35	J045147.22+450757.0	72.947	45.133	160.632	0.577	0.17	-44.96	10.23	13.21 ± 0.02	12.24 ± 0.02	11.81 ± 0.02	0.95	0.98	E/S0	—
36	J045117.73+451208.6	72.824	45.202	160.523	0.555	0.25	35.05	9.63	13.37 ± 0.02	12.35 ± 0.02	11.82 ± 0.02	1.01	1.12	E/S0	—
37	J045132.32+442920.1	72.885	44.489	161.100	0.133	0.73	-87.70	16.54	13.36 ± 0.02	12.43 ± 0.02	11.85 ± 0.02	0.76	1.18	eS	5129
38	J044918.07+445318.3	72.325	44.888	160.538	0.083	0.21	-18.37	10.40	13.23 ± 0.02	12.26 ± 0.02	11.86 ± 0.02	0.90	0.98	eS	—
39	J044941.69+452719.7	72.424	45.455	160.148	0.500	0.18	-13.54	8.04	13.42 ± 0.02	12.42 ± 0.02	11.86 ± 0.02	1.04	1.11	eS	—

Table B – Continued

ID no.	Unique ID	RA	Dec	ℓ	b	ϵ_K	ϕ_K	r_{K20}	J_{K20}	H_{K20}	K_{K20}	$E(B-V)$	J^0-K^0	Type	v_{rad}
	ZoA	deg	deg	deg	deg		deg	"	mag	mag	mag	mag	mag		km s ⁻¹
(1)	(2)	(3)	(4)	(5)	(6)	(7)	(8)	(9)	(10)	(11)	(12)	(13)	(14)	(15)	(16)
40	J045021.54+450047.4	72.590	45.013	160.563	0.307	0.53	-84.10	13.27	13.43 ± 0.02	12.39 ± 0.02	11.90 ± 0.02	0.98	1.10	eS	—
41	J044558.57+441637.7	71.494	44.277	160.623	-0.764	0.55	-11.81	17.24	13.30 ± 0.02	12.31 ± 0.02	11.91 ± 0.02	0.85	1.03	eS	—
42	J045135.55+450302.9	72.898	45.051	160.673	0.499	0.50	54.65	10.20	13.39 ± 0.02	12.43 ± 0.02	11.95 ± 0.02	0.95	1.03	E/SO	—
43	J044913.04+443545.2	72.304	44.596	160.753	-0.116	0.48	4.20	9.99	13.45 ± 0.02	12.55 ± 0.02	12.14 ± 0.02	0.78	0.97	E/SO	—
44	J045005.82+453012.6	72.524	45.503	160.156	0.585	0.23	18.87	10.69	13.69 ± 0.02	12.72 ± 0.02	12.14 ± 0.02	1.09	1.08	mS	—
45	J044940.15+445844.4	72.417	44.979	160.511	0.191	0.64	7.97	14.62	13.63 ± 0.02	12.63 ± 0.02	12.17 ± 0.02	0.94	1.05	eS	—
46	J045134.83+452431.0	72.895	45.409	160.395	0.725	0.12	-70.79	10.37	13.68 ± 0.02	12.66 ± 0.02	12.18 ± 0.02	1.05	1.05	E/SO	—
47	J045217.59+443511.6	73.073	44.587	161.110	0.299	0.46	-36.63	9.46	13.53 ± 0.02	12.62 ± 0.02	12.19 ± 0.02	0.76	1.02	E/SO	—
48	J044747.17+444434.0	71.947	44.743	160.477	-0.216	0.50	10.00	12.70	13.59 ± 0.05	12.61 ± 0.06	12.20 ± 0.07	0.88	1.01	eS	—
49	J044935.63+450035.3	72.398	45.010	160.479	0.201	0.40	60.58	10.79	13.67 ± 0.02	12.65 ± 0.02	12.21 ± 0.02	0.95	1.05	eS	—
50	J044956.71+451705.5	72.486	45.285	160.307	0.425	0.17	56.59	11.24	13.81 ± 0.02	12.71 ± 0.02	12.26 ± 0.02	1.04	1.10	E/SO	—
51	J045018.81+451136.0	72.578	45.193	160.419	0.416	0.47	-47.84	10.04	13.83 ± 0.02	12.79 ± 0.02	12.28 ± 0.02	1.02	1.11	eS	—
52	J044557.04+450410.9	71.488	45.070	160.017	-0.252	0.09	-21.67	8.27	13.78 ± 0.02	12.78 ± 0.02	12.35 ± 0.02	0.98	1.01	E/SO	—
53	J044820.62+453134.0	72.086	45.526	159.942	0.364	0.51	53.15	10.89	13.84 ± 0.02	12.83 ± 0.02	12.38 ± 0.02	1.04	1.01	E/SO	—
54	J044608.05+441621.5	71.534	44.273	160.644	-0.745	0.75	-11.80	14.15	13.93 ± 0.02	12.96 ± 0.02	12.48 ± 0.02	0.84	1.09	eS	—
55	J045303.58+442506.5	73.265	44.418	161.327	0.298	0.68	-3.61	12.52	13.80 ± 0.02	12.92 ± 0.02	12.50 ± 0.02	0.78	0.97	eS	—
56	J044934.14+443426.7	72.392	44.574	160.810	-0.082	0.44	35.56	14.58	13.84 ± 0.02	12.91 ± 0.02	12.52 ± 0.02	0.76	0.99	mS	—
57	J045038.23+450521.6	72.659	45.089	160.535	0.393	0.36	47.90	6.84	14.07 ± 0.02	13.09 ± 0.02	12.54 ± 0.02	1.00	1.10	E/SO	—
58	J045125.48+452551.4	72.856	45.431	160.361	0.718	0.52	79.07	12.39	14.08 ± 0.02	13.04 ± 0.02	12.54 ± 0.02	1.09	1.06	mS	—
59	J044949.59+450319.7	72.457	45.055	160.470	0.262	0.20	-30.00	8.50	14.07 ± 0.07	13.03 ± 0.06	12.57 ± 0.08	0.96	1.08	E/SO	—
60	J045401.51+451426.6	73.506	45.241	160.798	0.951	0.55	-61.16	9.67	14.01 ± 0.02	13.01 ± 0.02	12.57 ± 0.02	0.98	1.02	eS	—
61	J045444.87+453116.6	73.687	45.521	160.660	1.226	0.50	51.50	13.71	13.94 ± 0.02	12.98 ± 0.02	12.57 ± 0.02	0.80	1.02	eS	—
62	J045233.08+445548.6	73.138	44.930	160.874	0.553	0.63	-57.68	8.91	14.06 ± 0.02	13.08 ± 0.02	12.59 ± 0.02	0.94	1.07	eS	—
63	J044646.93+441620.4	71.696	44.272	160.720	-0.657	0.61	-84.87	13.48	13.94 ± 0.02	12.99 ± 0.02	12.60 ± 0.02	0.74	1.01	mS	—
64	J044801.07+444319.3	72.004	44.722	160.519	-0.198	0.26	24.21	7.83	14.05 ± 0.02	13.08 ± 0.02	12.64 ± 0.02	0.86	1.04	E/SO	—
65	J045040.23+445701.0	72.668	44.950	160.646	0.309	0.70	-67.23	14.57	14.07 ± 0.02	13.09 ± 0.02	12.68 ± 0.02	0.92	0.99	mS	—
66	J044409.43+443700.4	71.039	44.617	160.153	-0.788	0.40	-51.65	10.30	14.22 ± 0.02	13.18 ± 0.02	12.70 ± 0.02	1.09	1.06	mS	—
67	J044902.91+445639.9	72.262	44.944	160.467	0.085	0.07	-89.11	8.41	14.11 ± 0.02	13.16 ± 0.02	12.70 ± 0.02	0.90	1.03	eS	—
68	J044927.08+450121.8	72.363	45.023	160.452	0.190	0.29	-83.90	7.96	14.22 ± 0.02	13.18 ± 0.02	12.73 ± 0.02	0.95	1.08	E/SO	—
69	J045429.83+444425.9	73.624	44.741	161.239	0.700	0.38	-74.39	7.18	14.23 ± 0.02	13.23 ± 0.02	12.75 ± 0.02	0.87	1.10	eS	—
70	J045156.51+450314.5	72.985	45.054	160.710	0.548	0.40	30.50	10.67	14.16 ± 0.02	13.23 ± 0.02	12.80 ± 0.02	0.94	0.96	mS	4523
71	J044642.74+444225.2	71.678	44.707	160.381	-0.385	0.02	-69.65	5.85	14.25 ± 0.02	13.26 ± 0.02	12.80 ± 0.02	0.92	1.06	eS	—
72	J045031.44+453451.2	72.631	45.581	160.145	0.692	0.43	-20.20	8.32	14.37 ± 0.02	13.35 ± 0.02	12.86 ± 0.02	1.20	0.99	eS	—
73	J044741.94+445903.4	71.925	44.984	160.282	-0.072	0.36	17.96	8.27	14.24 ± 0.02	13.30 ± 0.02	12.87 ± 0.02	0.86	1.01	eS	—
74	J045030.71+442816.0	72.628	44.471	160.997	-0.019	0.35	45.97	8.77	14.15 ± 0.02	13.25 ± 0.02	12.87 ± 0.02	0.79	0.94	eS	—
75	J045149.06+450924.8	72.954	45.157	160.616	0.597	0.22	44.85	7.22	14.29 ± 0.02	13.33 ± 0.02	12.87 ± 0.02	0.93	1.03	E/SO	—
76	J044615.88+450530.3	71.566	45.092	160.036	-0.195	0.65	62.54	9.64	14.26 ± 0.02	13.44 ± 0.02	12.91 ± 0.02	0.94	0.94	eS	—
77	J044752.80+450202.3	71.970	45.034	160.265	-0.015	0.40	-40.00	9.50	14.26 ± 0.08	13.35 ± 0.08	12.91 ± 0.09	0.86	0.98	E/SO	—
78	J045005.99+444129.8	72.525	44.692	160.780	0.066	0.57	-84.01	7.73	14.31 ± 0.02	13.41 ± 0.02	12.97 ± 0.02	0.82	0.98	eS	—
79	J044707.90+442944.4	71.783	44.496	160.590	-0.465	0.10	-69.40	7.97	14.43 ± 0.02	13.54 ± 0.02	12.98 ± 0.02	0.78	1.11	E/SO	—

Table B – Continued

ID no.	Unique ID	RA	Dec	ℓ	b	ϵ_K	ϕ_K	r_{K20}	J_{K20}	H_{K20}	K_{K20}	$E(B-V)$	J^0-K^0	Type	v_{rad}
	ZoA	deg	deg	deg	deg	deg	deg	"	mag	mag	mag	mag	mag		km s ⁻¹
(1)	(2)	(3)	(4)	(5)	(6)	(7)	(8)	(9)	(10)	(11)	(12)	(13)	(14)	(15)	(16)
80	J044918.88+454737.1	72.329	45.794	159.846	0.666	0.21	-51.00	9.01	14.60 ± 0.02	13.56 ± 0.02	12.98 ± 0.02	1.14	1.12	<i>mS</i>	—
81	J045418.02+453951.7	73.575	45.664	160.499	1.255	0.39	49.59	9.30	14.35 ± 0.02	13.41 ± 0.02	13.00 ± 0.02	0.88	0.96	<i>mS</i>	—
82	J045353.83+443238.8	73.474	44.544	161.324	0.494	0.37	37.88	8.88	14.45 ± 0.02	13.51 ± 0.02	13.02 ± 0.02	0.85	1.07	<i>eS</i>	—
83	J045146.37+452706.8	72.943	45.452	160.384	0.778	0.59	79.33	8.71	14.54 ± 0.02	13.53 ± 0.02	13.04 ± 0.02	1.13	1.01	<i>eS</i>	—
84	J044520.92+454430.7	71.337	45.742	159.440	0.110	0.77	24.83	14.61	14.94 ± 0.02	13.68 ± 0.02	13.05 ± 0.02	1.28	1.33	<i>mS</i>	5134
85	J045206.26+451041.6	73.026	45.178	160.632	0.649	0.23	-75.26	6.58	14.51 ± 0.02	13.48 ± 0.02	13.05 ± 0.02	0.90	1.07	E/S0	—
86	J044859.13+450201.1	72.246	45.034	160.391	0.134	0.22	-23.15	6.11	14.55 ± 0.02	13.54 ± 0.02	13.06 ± 0.02	0.93	1.08	E/S0	—
87	J045022.58+451600.9	72.594	45.267	160.370	0.472	0.26	65.62	6.78	14.66 ± 0.02	13.54 ± 0.02	13.06 ± 0.02	1.03	1.16	E/S0	—
88	J044848.38+450140.8	72.202	45.028	160.375	0.106	0.48	-43.50	8.56	14.60 ± 0.02	13.54 ± 0.02	13.11 ± 0.02	0.90	1.09	<i>mS</i>	—
89	J044941.44+445807.9	72.423	44.969	160.521	0.188	0.21	-34.30	6.52	14.52 ± 0.02	13.55 ± 0.02	13.12 ± 0.02	0.94	1.00	E/S0	—
90	J044922.34+444427.2	72.343	44.741	160.660	-0.002	0.08	-15.60	6.15	14.55 ± 0.02	13.59 ± 0.02	13.17 ± 0.02	0.84	1.01	<i>eS</i>	—
91	J044812.49+450920.1	72.052	45.156	160.210	0.107	0.24	-45.33	7.28	14.60 ± 0.02	13.61 ± 0.02	13.20 ± 0.02	0.94	0.99	<i>eS</i>	—
92	J044743.67+445439.8	71.932	44.911	160.342	-0.115	0.41	-69.81	7.60	14.56 ± 0.02	13.68 ± 0.02	13.21 ± 0.02	0.84	0.98	<i>eS</i>	—
93	J045131.32+450558.1	72.880	45.099	160.627	0.520	0.03	-16.62	6.54	14.74 ± 0.02	13.72 ± 0.02	13.25 ± 0.02	0.95	1.07	E/S0	—
94	J044944.65+452304.9	72.436	45.385	160.208	0.462	0.37	-41.69	7.31	14.70 ± 0.02	13.70 ± 0.02	13.26 ± 0.02	1.06	0.99	<i>eS</i>	—
95	J044933.20+445558.6	72.388	44.933	160.533	0.146	0.10	-56.04	4.90	14.75 ± 0.02	13.76 ± 0.02	13.28 ± 0.02	0.94	1.06	E/S0	—
96	J044935.99+445213.7	72.400	44.870	160.586	0.112	0.24	2.46	6.83	14.75 ± 0.02	13.73 ± 0.02	13.30 ± 0.02	0.93	1.05	E/S0	—
97	J044943.68+443245.1	72.432	44.546	160.850	-0.078	0.16	-59.70	5.72	14.63 ± 0.02	13.73 ± 0.02	13.35 ± 0.02	0.75	0.97	<i>eS</i>	—
98	J045216.50+441218.2	73.069	44.205	161.403	0.055	0.27	-3.60	6.37	14.72 ± 0.02	13.77 ± 0.02	13.35 ± 0.02	0.63	1.10	E/S0	—
99	J044947.45+450944.5	72.448	45.162	160.384	0.325	0.43	-44.49	7.29	14.89 ± 0.02	13.88 ± 0.02	13.37 ± 0.02	0.98	1.10	<i>eS</i>	—
100	J044417.15+443615.4	71.071	44.604	160.178	-0.779	0.50	-50.00	9.40	14.98 ± 0.11	13.80 ± 0.09	13.46 ± 0.12	1.09	1.04	<i>mS</i>	—
101	J045226.36+451011.7	73.110	45.170	160.676	0.690	0.39	21.47	6.53	14.89 ± 0.02	13.93 ± 0.02	13.47 ± 0.02	0.87	1.05	E/S0	—
102	J045216.79+455402.2	73.070	45.901	160.093	1.132	0.52	-17.24	7.05	14.93 ± 0.02	13.96 ± 0.02	13.49 ± 0.02	1.02	1.00	<i>mS</i>	—
103	J045301.01+442921.2	73.254	44.489	161.267	0.337	0.39	34.50	7.43	14.92 ± 0.02	13.97 ± 0.02	13.50 ± 0.02	0.80	1.08	<i>mS</i>	—
104	J045314.91+452642.6	73.312	45.445	160.553	0.974	0.49	-74.74	6.44	14.98 ± 0.02	13.98 ± 0.02	13.54 ± 0.02	0.98	1.02	E/S0	—
105	J044650.13+452342.0	71.709	45.395	159.871	0.078	0.45	65.44	7.23	15.07 ± 0.02	14.04 ± 0.02	13.55 ± 0.02	1.13	1.03	<i>eS</i>	—
106	J045004.69+450036.1	72.520	45.010	160.533	0.267	0.34	31.33	4.94	15.09 ± 0.02	14.08 ± 0.02	13.57 ± 0.02	0.97	1.10	E/S0	—
107	J045100.26+445855.4	72.751	44.982	160.659	0.375	0.24	36.21	4.72	15.04 ± 0.02	14.05 ± 0.02	13.62 ± 0.02	0.91	1.03	E/S0	—
108	J044959.35+445647.7	72.497	44.947	160.572	0.214	0.33	-53.30	6.69	15.11 ± 0.02	14.13 ± 0.02	13.65 ± 0.02	0.97	1.04	<i>mS</i>	—
109	J045432.63+451846.8	73.636	45.313	160.799	1.067	0.16	-0.60	3.03	15.19 ± 0.02	14.23 ± 0.02	13.67 ± 0.02	0.90	1.14	E/S0	—
110	J045445.42+453911.3	73.689	45.653	160.560	1.310	0.48	-39.85	9.48	14.87 ± 0.02	14.01 ± 0.02	13.73 ± 0.03	0.84	0.77	<i>mS</i>	4941
111	J045143.42+454722.1	72.931	45.789	160.118	0.987	0.26	-66.54	3.51	15.37 ± 0.02	14.40 ± 0.02	13.77 ± 0.02	1.34	1.02	E/S0	—
112	J044900.93+441937.0	72.254	44.327	160.936	-0.316	0.69	-85.32	9.15	15.20 ± 0.02	14.27 ± 0.02	13.81 ± 0.03	0.64	1.11	<i>mS</i>	6332
113	J044555.95+444549.4	71.483	44.764	160.248	-0.453	0.24	70.62	6.78	15.19 ± 0.02	14.23 ± 0.02	13.81 ± 0.03	0.99	0.95	<i>mS</i>	—
114	J045403.78+443621.7	73.516	44.606	161.294	0.556	0.49	-43.64	6.81	15.12 ± 0.02	14.20 ± 0.02	13.81 ± 0.02	0.87	0.94	<i>mS</i>	—
115	J044823.57+451244.2	72.098	45.212	160.187	0.169	0.03	41.98	5.03	15.23 ± 0.02	14.28 ± 0.02	13.82 ± 0.02	0.98	0.99	<i>mS</i>	—
116	J045105.62+443545.0	72.773	44.596	160.970	0.140	0.05	38.79	5.25	14.93 ± 0.02	14.18 ± 0.02	13.87 ± 0.03	0.77	0.73	<i>mS</i>	5044
117	J045156.82+453619.8	72.987	45.606	160.284	0.900	0.12	-0.68	4.67	15.62 ± 0.02	14.53 ± 0.02	13.88 ± 0.02	1.62	1.04	E/S0	—
118	J044920.79+450159.4	72.337	45.033	160.433	0.183	0.50	-60.00	7.60	15.25 ± 0.13	14.00 ± 0.09	13.89 ± 0.14	0.95	0.95	<i>mS</i>	—
119	J045029.63+441012.4	72.623	44.170	161.226	-0.214	0.15	2.40	6.40	15.15 ± 0.02	14.31 ± 0.02	13.92 ± 0.03	0.64	0.96	<i>mS</i>	—

Table B – Continued

ID no.	Unique ID	RA	Dec	ℓ	b	ϵ_K	ϕ_K	r_{K20}	J_{K20}	H_{K20}	K_{K20}	$E(B-V)$	J^0-K^0	Type	v_{rad}
	ZoA	deg	deg	deg	deg		deg	"	mag	mag	mag	mag	mag		km s ⁻¹
(1)	(2)	(3)	(4)	(5)	(6)	(7)	(8)	(9)	(10)	(11)	(12)	(13)	(14)	(15)	(16)
120	J044706.52+451102.1	71.777	45.184	160.063	-0.022	0.07	-35.59	3.95	15.36 ± 0.02	14.40 ± 0.02	13.94 ± 0.02	0.94	1.01	E/S0	—
121	J044950.94+454506.7	72.462	45.752	159.938	0.711	0.14	-35.38	4.73	15.53 ± 0.02	14.48 ± 0.02	13.94 ± 0.02	1.15	1.09	E/S0	—
122	J044434.42+445034.2	71.143	44.843	160.031	-0.584	0.10	9.12	3.65	15.44 ± 0.02	14.40 ± 0.02	13.96 ± 0.02	1.11	1.01	E/S0	—
123	J044946.26+450747.6	72.443	45.130	160.406	0.302	0.49	24.10	6.81	15.45 ± 0.02	14.37 ± 0.02	13.97 ± 0.03	0.98	1.07	mS	—
124	J044658.40+452255.0	71.743	45.382	159.896	0.088	0.07	-35.86	4.02	15.61 ± 0.02	14.62 ± 0.02	13.99 ± 0.02	1.11	1.14	E/S0	—
125	J044816.56+451604.5	72.069	45.268	160.131	0.189	0.01	-39.80	4.12	15.38 ± 0.02	14.43 ± 0.02	14.00 ± 0.02	1.02	0.94	E/S0	—
126	J045042.89+445937.4	72.679	44.994	160.618	0.343	0.32	-63.47	5.81	15.48 ± 0.02	14.43 ± 0.02	14.00 ± 0.02	0.93	1.07	mS	—
127	J044403.24+443827.5	71.014	44.641	160.123	-0.786	0.00	90.00	5.90	15.56 ± 0.16	14.36 ± 0.13	14.02 ± 0.17	1.10	1.06	mS	—
128	J045021.00+451216.6	72.587	45.205	160.414	0.428	0.26	-72.94	5.67	15.53 ± 0.02	14.49 ± 0.02	14.02 ± 0.02	1.02	1.07	mS	—
129	J045029.29+460723.4	72.622	46.123	159.724	1.034	0.28	49.67	5.21	15.57 ± 0.02	14.62 ± 0.02	14.02 ± 0.02	0.99	1.13	E/S0	—
130	J044646.85+452209.9	71.695	45.369	159.884	0.054	0.09	-26.10	4.14	15.59 ± 0.02	14.60 ± 0.02	14.03 ± 0.02	1.10	1.09	E/S0	—
131	J045419.04+452229.0	73.579	45.375	160.726	1.075	0.20	72.14	5.28	15.48 ± 0.02	14.53 ± 0.02	14.03 ± 0.02	0.93	1.04	mS	—
132	J045416.62+452530.8	73.569	45.425	160.682	1.102	0.00	90.00	5.00	15.42 ± 0.14	14.49 ± 0.14	14.07 ± 0.16	0.90	0.96	eS	—
133	J044721.08+450806.7	71.838	45.135	160.128	-0.021	0.25	-58.10	5.70	15.47 ± 0.02	14.50 ± 0.02	14.09 ± 0.03	0.90	0.99	mS	—
134	J045002.01+450215.3	72.508	45.038	160.507	0.278	0.48	55.19	6.12	15.54 ± 0.02	14.54 ± 0.02	14.09 ± 0.02	0.98	1.03	eS	—
135	J045541.23+445953.2	73.922	44.998	161.171	1.026	0.33	-54.60	5.30	15.60 ± 0.02	14.64 ± 0.02	14.11 ± 0.02	0.90	1.11	eS	—
136	J044802.83+452237.9	72.012	45.377	160.022	0.229	0.17	22.56	4.32	15.71 ± 0.02	14.76 ± 0.02	14.12 ± 0.02	1.07	1.13	E/S0	—
137	J044524.63+451918.2	71.353	45.322	159.764	-0.160	0.02	-32.18	4.01	15.60 ± 0.02	14.71 ± 0.02	14.13 ± 0.03	1.14	0.98	mS	6830
138	J044908.53+450705.9	72.286	45.118	160.344	0.209	0.12	26.00	5.19	15.57 ± 0.02	14.58 ± 0.02	14.14 ± 0.03	0.96	1.02	mS	—
139	J044755.58+450438.2	71.982	45.077	160.237	0.019	0.43	-62.81	5.82	15.52 ± 0.02	14.55 ± 0.02	14.15 ± 0.03	0.88	1.00	mS	—
140	J045029.48+450139.1	72.623	45.028	160.567	0.334	0.15	-24.88	3.98	15.66 ± 0.02	14.65 ± 0.02	14.15 ± 0.02	0.97	1.09	Irr	—
141	J045026.25+445346.6	72.609	44.896	160.661	0.243	0.04	42.27	4.30	15.56 ± 0.02	14.64 ± 0.02	14.18 ± 0.02	0.93	0.98	E/S0	—
142	J044616.70+440932.4	71.570	44.159	160.748	-0.799	0.17	26.77	4.30	15.52 ± 0.02	14.62 ± 0.02	14.19 ± 0.03	0.79	0.99	mS	—
143	J044632.01+440858.6	71.633	44.150	160.784	-0.770	0.00	90.00	5.00	15.53 ± 0.14	14.43 ± 0.04	14.21 ± 0.17	0.75	1.00	eS	—
144	J044603.60+444430.9	71.515	44.742	160.279	-0.450	0.09	-5.20	4.19	15.61 ± 0.02	14.62 ± 0.02	14.24 ± 0.03	0.99	0.93	mS	—
145	J044357.81+443721.5	70.991	44.623	160.126	-0.810	0.48	81.34	5.71	15.74 ± 0.02	14.74 ± 0.02	14.25 ± 0.03	1.09	1.03	mS	—
146	J045159.93+451925.2	73.000	45.324	160.508	0.728	0.58	8.91	6.35	15.66 ± 0.02	14.69 ± 0.02	14.25 ± 0.03	0.99	0.98	eS	—
147	J045229.45+452451.7	73.123	45.414	160.493	0.852	0.59	-19.33	6.61	15.66 ± 0.02	14.72 ± 0.02	14.25 ± 0.02	0.98	0.99	mS	—
148	J044728.19+450836.8	71.867	45.144	160.135	0.000	0.49	88.14	6.20	15.63 ± 0.02	14.71 ± 0.02	14.26 ± 0.03	0.95	0.95	ℓS	—
149	J045409.86+445915.6	73.541	44.988	161.010	0.810	0.42	-78.78	6.35	15.66 ± 0.02	14.73 ± 0.02	14.28 ± 0.03	0.91	1.00	E/S0	—
150	J044944.04+452717.6	72.434	45.455	160.153	0.505	0.28	-69.33	3.95	15.88 ± 0.02	14.92 ± 0.02	14.32 ± 0.02	1.04	1.11	E/S0	—
151	J044456.88+453304.0	71.237	45.551	159.537	-0.072	0.04	-58.90	4.28	16.03 ± 0.03	14.95 ± 0.02	14.33 ± 0.03	1.35	1.12	E/S0	—
152	J045213.66+455728.1	73.057	45.958	160.043	1.161	0.38	-41.73	4.79	15.89 ± 0.02	14.96 ± 0.02	14.35 ± 0.03	1.04	1.09	E/S0	—
153	J045253.13+443406.9	73.221	44.569	161.191	0.369	0.36	78.70	5.33	15.76 ± 0.02	14.84 ± 0.02	14.36 ± 0.03	0.78	1.05	ℓS	—
154	J044744.15+441950.0	71.934	44.331	160.786	-0.489	0.60	-18.30	6.04	15.63 ± 0.02	14.83 ± 0.02	14.42 ± 0.03	0.70	0.90	ℓS	4878
155	J044434.53+452801.4	71.144	45.467	159.558	-0.176	0.19	-44.80	3.98	16.13 ± 0.02	15.09 ± 0.02	14.44 ± 0.03	1.30	1.13	mS	—
156	J045238.00+453139.1	73.158	45.528	160.421	0.943	0.30	16.90	3.91	15.94 ± 0.02	14.93 ± 0.02	14.44 ± 0.02	1.17	0.99	eS	—
157	J044926.79+445532.2	72.362	44.926	160.526	0.127	0.67	-51.10	7.25	15.81 ± 0.02	14.92 ± 0.02	14.45 ± 0.03	0.92	0.96	mS	—
158	J044651.22+442147.3	71.713	44.363	160.659	-0.588	0.06	-23.49	4.07	15.86 ± 0.03	15.03 ± 0.02	14.48 ± 0.03	0.73	1.07	E/S0	—
159	J045216.28+451657.3	73.068	45.283	160.570	0.738	0.20	34.80	4.58	15.96 ± 0.03	15.02 ± 0.02	14.52 ± 0.03	0.92	1.04	mS	—

Table B – Continued

ID no.	Unique ID	RA	Dec	ℓ	b	ϵ_K	ϕ_K	r_{K20}	J_{K20}	H_{K20}	K_{K20}	$E(B-V)$	J^0-K^0	Type	v_{rad}
	ZoA	deg	deg	deg	deg	deg	deg	"	mag	mag	mag	mag	mag		km s ⁻¹
(1)	(2)	(3)	(4)	(5)	(6)	(7)	(8)	(9)	(10)	(11)	(12)	(13)	(14)	(15)	(16)
160	J044858.75+441329.9	72.245	44.225	161.010	-0.387	0.47	-82.16	4.88	15.89 ± 0.02	14.98 ± 0.02	14.57 ± 0.03	0.67	1.03	ℓ S	—
161	J044947.40+444454.6	72.447	44.749	160.701	0.060	0.67	16.72	6.49	15.96 ± 0.03	14.99 ± 0.02	14.59 ± 0.03	0.86	1.00	m S	—
162	J045224.39+451948.4	73.102	45.330	160.548	0.787	0.39	-64.60	4.15	16.01 ± 0.02	15.11 ± 0.02	14.60 ± 0.03	0.94	1.01	E/SO	—
163	J045012.16+445802.4	72.551	44.967	160.580	0.256	0.57	18.53	6.47	16.12 ± 0.03	15.08 ± 0.02	14.61 ± 0.03	0.97	1.09	e S	—
164	J044621.16+441634.4	71.588	44.276	160.667	-0.713	0.49	-5.56	4.98	15.90 ± 0.02	15.00 ± 0.02	14.62 ± 0.03	0.81	0.93	m S	—
165	J045532.82+450602.8	73.887	45.101	161.075	1.071	0.24	-51.61	3.82	16.05 ± 0.02	15.09 ± 0.02	14.63 ± 0.03	0.91	1.03	m S	—
166	J044858.41+451309.8	72.243	45.219	160.248	0.252	0.10	-46.62	4.23	16.21 ± 0.03	15.16 ± 0.02	14.69 ± 0.03	0.96	1.11	m S	—
167	J045011.73+445955.1	72.549	44.999	160.555	0.275	0.41	51.90	4.58	16.12 ± 0.02	15.12 ± 0.02	14.70 ± 0.03	0.98	1.00	m S	—
168	J044651.60+455551.6	71.715	45.931	159.465	0.428	0.30	-7.58	4.66	16.34 ± 0.03	15.33 ± 0.03	14.71 ± 0.03	1.22	1.11	e S	—
169	J044739.96+443348.7	71.917	44.564	160.600	-0.348	0.38	46.20	5.61	16.07 ± 0.03	15.09 ± 0.02	14.72 ± 0.03	0.84	0.98	Irr	—
170	J044406.51+445621.7	71.027	44.939	159.904	-0.584	0.33	10.47	4.93	16.27 ± 0.03	15.19 ± 0.02	14.75 ± 0.03	1.15	1.02	m S	—
171	J044541.16+454528.0	71.421	45.758	159.464	0.160	0.19	-38.51	3.12	16.40 ± 0.03	15.37 ± 0.02	14.75 ± 0.03	1.26	1.11	E/SO	—
172	J044645.56+450429.6	71.690	45.075	160.106	-0.140	0.36	84.91	5.14	16.07 ± 0.03	15.12 ± 0.02	14.76 ± 0.03	0.88	0.94	e S	—
173	J045255.84+454914.2	73.233	45.821	160.227	1.169	0.22	-59.55	3.79	16.14 ± 0.03	15.17 ± 0.02	14.76 ± 0.03	0.96	0.97	e S	—
174	J045251.64+441648.4	73.215	44.280	161.411	0.183	0.25	-14.71	3.83	15.99 ± 0.02	15.11 ± 0.02	14.77 ± 0.03	0.66	0.94	E/SO	—
175	J044708.49+450527.2	71.785	45.091	160.137	-0.078	0.09	75.04	3.10	16.07 ± 0.02	15.13 ± 0.02	14.79 ± 0.03	0.88	0.90	E/SO	—
176	J045433.21+445344.2	73.638	44.896	161.124	0.806	0.22	-27.96	3.42	16.30 ± 0.03	15.34 ± 0.02	14.80 ± 0.03	0.89	1.12	E/SO	—
177	J045441.39+451904.9	73.672	45.318	160.811	1.090	0.35	-37.70	3.06	16.31 ± 0.02	15.59 ± 0.02	14.81 ± 0.03	0.89	1.11	e S	—
178	J044838.24+445640.2	72.159	44.945	160.420	0.029	0.09	-68.89	3.45	16.11 ± 0.02	15.20 ± 0.02	14.82 ± 0.03	0.86	0.92	E/SO	—
179	J044614.90+452745.3	71.562	45.463	159.753	0.043	0.29	13.74	3.22	16.50 ± 0.03	15.47 ± 0.02	14.85 ± 0.03	1.23	1.11	m S	—
180	J045013.36+440839.0	72.556	44.144	161.210	-0.270	0.44	79.01	4.57	15.91 ± 0.02	15.21 ± 0.02	14.87 ± 0.03	0.63	0.78	Irr	5547
181	J044938.32+435622.7	72.410	43.940	161.305	-0.479	0.07	-73.58	3.12	16.23 ± 0.03	15.36 ± 0.03	14.89 ± 0.03	0.62	1.07	E/SO	—
182	J044953.62+450543.4	72.473	45.095	160.447	0.296	0.12	82.40	3.15	16.38 ± 0.02	15.38 ± 0.02	14.90 ± 0.03	0.99	1.05	m S	—
183	J045123.45+460416.4	72.848	46.071	159.863	1.121	0.47	-66.91	4.71	16.38 ± 0.03	15.37 ± 0.02	14.90 ± 0.03	1.02	1.04	ℓ S	—
184	J045440.78+445807.9	73.670	44.969	161.082	0.869	0.23	80.85	2.66	16.37 ± 0.02	15.44 ± 0.02	14.90 ± 0.03	0.91	1.07	E/SO	—
185	J044921.23+460126.8	72.338	46.024	159.674	0.820	0.33	6.21	3.62	16.49 ± 0.03	15.39 ± 0.03	14.92 ± 0.03	1.17	1.07	Irr	—
186	J044738.78+450532.7	71.912	45.092	160.194	-0.009	0.21	-64.50	3.95	16.35 ± 0.03	15.35 ± 0.02	14.94 ± 0.03	0.87	1.03	ℓ S	—
187	J044855.57+443933.7	72.232	44.659	160.671	-0.115	0.72	4.90	8.79	16.39 ± 0.03	15.49 ± 0.03	14.94 ± 0.04	0.80	1.10	m S	—
188	J044543.46+450440.7	71.431	45.078	159.985	-0.277	0.36	-80.84	4.44	16.34 ± 0.03	15.36 ± 0.02	14.95 ± 0.03	1.03	0.95	ℓ S	—
189	J044952.70+451451.0	72.470	45.247	160.328	0.392	0.24	65.67	4.62	16.50 ± 0.03	15.57 ± 0.03	14.98 ± 0.03	1.00	1.09	Irr	—
190	J044957.62+440316.6	72.490	44.055	161.254	-0.361	0.33	11.46	4.17	16.18 ± 0.03	15.36 ± 0.02	14.98 ± 0.03	0.64	0.93	ℓ S	—
191	J044810.67+444742.0	72.044	44.795	160.482	-0.129	0.38	32.80	3.89	16.40 ± 0.03	15.46 ± 0.03	14.99 ± 0.04	0.82	1.05	m S	—
192	J044856.82+444953.0	72.237	44.831	160.542	-0.002	0.09	75.80	3.55	16.35 ± 0.03	15.37 ± 0.03	15.03 ± 0.03	0.83	0.96	ℓ S	—
193	J044507.40+450214.4	71.281	45.037	159.947	-0.384	0.34	-30.50	4.18	16.51 ± 0.03	15.52 ± 0.03	15.05 ± 0.03	1.12	0.98	ℓ S	—
194	J045420.33+451848.0	73.585	45.313	160.776	1.039	0.61	53.91	5.80	16.43 ± 0.03	15.50 ± 0.02	15.05 ± 0.03	0.92	0.98	e S	—
195	J045443.36+444708.1	73.681	44.786	161.229	0.760	0.47	-58.34	4.83	16.47 ± 0.03	15.55 ± 0.03	15.05 ± 0.04	0.88	1.03	m S	—
196	J044955.20+451139.7	72.480	45.194	160.374	0.363	0.03	-6.91	3.08	16.45 ± 0.03	15.47 ± 0.02	15.07 ± 0.03	0.99	0.96	ℓ S	—
197	J044737.90+451002.9	71.908	45.167	160.135	0.037	0.23	34.62	2.81	16.59 ± 0.03	15.85 ± 0.03	15.09 ± 0.03	0.94	1.09	ℓ S	—
198	J044852.61+445740.8	72.219	44.961	160.434	0.073	0.23	-14.44	3.24	16.47 ± 0.03	15.51 ± 0.02	15.10 ± 0.03	0.89	0.98	ℓ S	—
199	J044547.35+454302.2	71.447	45.717	159.507	0.148	0.61	43.30	5.75	16.72 ± 0.03	15.77 ± 0.03	15.12 ± 0.04	1.27	1.05	e S	—

Table B – Continued

ID no.	Unique ID	RA	Dec	ℓ	b	ϵ_K	ϕ_K	r_{K20}	J_{K20}	H_{K20}	K_{K20}	$E(B-V)$	J^0-K^0	Type	v_{rad}
	ZoA	deg	deg	deg	deg		deg	"	mag	mag	mag	mag	mag		km s ⁻¹
(1)	(2)	(3)	(4)	(5)	(6)	(7)	(8)	(9)	(10)	(11)	(12)	(13)	(14)	(15)	(16)
200	J044622.17+453307.3	71.592	45.552	159.698	0.117	0.46	-73.56	4.31	16.77 ± 0.03	15.76 ± 0.03	15.16 ± 0.04	1.28	1.06	ℓ S	—
201	J044545.92+444901.9	71.441	44.817	160.188	-0.441	0.11	67.60	4.00	16.62 ± 0.03	15.75 ± 0.03	15.21 ± 0.04	1.05	0.95	ℓ S	5134
202	J045012.70+453746.5	72.553	45.630	160.072	0.681	0.21	-58.70	3.14	16.78 ± 0.03	15.76 ± 0.03	15.21 ± 0.03	1.14	1.08	ℓ S	—
203	J045004.97+450154.3	72.521	45.032	160.517	0.281	0.34	-22.89	3.77	16.67 ± 0.03	15.69 ± 0.02	15.24 ± 0.03	0.97	1.01	ℓ S	—
204	J044617.48+452600.3	71.573	45.433	159.780	0.030	0.23	-8.24	4.19	16.87 ± 0.04	15.83 ± 0.03	15.28 ± 0.04	1.20	1.07	Irr	—
205	J045311.77+453648.0	73.299	45.613	160.417	1.074	0.18	22.04	3.19	16.73 ± 0.03	15.73 ± 0.02	15.31 ± 0.03	1.10	0.94	Irr	—
206	J045329.73+443729.2	73.374	44.625	161.216	0.489	0.61	73.06	4.40	16.66 ± 0.03	15.71 ± 0.02	15.32 ± 0.04	0.85	0.97	m S	—
207	J044445.84+444702.1	71.191	44.784	160.097	-0.597	0.20	10.23	3.97	16.90 ± 0.04	15.94 ± 0.03	15.33 ± 0.05	1.11	1.09	Irr	—
208	J045127.65+450922.6	72.865	45.156	160.577	0.548	0.56	56.41	4.66	16.82 ± 0.03	15.88 ± 0.03	15.35 ± 0.03	0.97	1.06	m S	—
209	J044955.57+454444.8	72.482	45.746	159.951	0.717	0.47	17.14	3.51	17.00 ± 0.03	16.01 ± 0.03	15.42 ± 0.03	1.16	1.09	ℓ S	—
210	J044437.62+443619.0	71.157	44.605	160.217	-0.732	0.28	25.70	3.64	16.93 ± 0.03	15.90 ± 0.03	15.44 ± 0.04	1.04	1.04	Irr	—
211	J045330.45+444657.0	73.377	44.783	161.095	0.590	0.53	0.35	4.16	16.82 ± 0.03	15.84 ± 0.03	15.44 ± 0.04	0.97	0.96	e S	—
212	J044756.88+442015.1	71.987	44.338	160.805	-0.456	0.20	66.40	3.21	16.75 ± 0.03	15.89 ± 0.03	15.45 ± 0.04	0.69	1.00	Irr	—
213	J044958.64+450152.9	72.494	45.031	160.505	0.267	0.31	-62.00	2.79	16.90 ± 0.03	15.87 ± 0.02	15.45 ± 0.03	0.96	1.03	E/SO	—
214	J045225.84+451456.9	73.108	45.249	160.614	0.739	0.00	-7.64	3.17	16.85 ± 0.03	15.87 ± 0.03	15.48 ± 0.04	0.90	0.99	Irr	—
215	J044531.48+443550.4	71.381	44.597	160.327	-0.617	0.12	-17.07	2.91	16.96 ± 0.03	15.98 ± 0.03	15.49 ± 0.04	1.04	1.02	ℓ S	—
216	J044638.07+444609.2	71.659	44.769	160.324	-0.355	0.53	-89.04	4.01	17.01 ± 0.03	16.05 ± 0.03	15.53 ± 0.04	0.91	1.09	e S	—
217	J044744.40+445626.1	71.935	44.941	160.321	-0.095	0.18	-5.80	2.80	16.89 ± 0.03	15.99 ± 0.03	15.53 ± 0.04	0.85	1.00	Irr	—
218	J044922.06+453019.4	72.342	45.505	160.073	0.488	0.01	42.10	2.83	16.98 ± 0.03	16.04 ± 0.03	15.54 ± 0.04	0.99	1.01	Irr	—
219	J045057.35+452532.4	72.739	45.426	160.312	0.651	0.14	9.90	3.04	17.04 ± 0.03	15.98 ± 0.03	15.54 ± 0.04	1.08	1.03	ℓ S	—
220	J044957.27+460315.1	72.489	46.054	159.720	0.920	0.44	19.55	4.28	16.93 ± 0.03	16.07 ± 0.03	15.56 ± 0.04	1.12	0.89	ℓ S	4942
221	J045241.41+452024.6	73.173	45.340	160.572	0.832	0.05	-62.10	2.92	16.91 ± 0.03	16.01 ± 0.03	15.56 ± 0.04	0.93	0.95	ℓ S	—
222	J044854.97+453243.7	72.229	45.545	159.991	0.454	0.06	-44.99	3.28	16.88 ± 0.03	16.01 ± 0.03	15.57 ± 0.04	0.97	0.89	Irr	—
223	J045243.81+443819.6	73.183	44.639	161.119	0.393	0.24	-26.00	3.20	16.89 ± 0.03	16.05 ± 0.03	15.57 ± 0.04	0.81	0.97	ℓ S	—
224	J045338.36+452459.0	73.410	45.416	160.619	1.009	0.12	-50.48	2.87	17.07 ± 0.03	16.22 ± 0.03	15.57 ± 0.03	0.92	1.10	Irr	—
225	J044959.00+442427.5	72.496	44.408	160.985	-0.132	0.34	39.37	2.94	16.85 ± 0.03	16.17 ± 0.03	15.62 ± 0.05	0.69	0.93	Irr	—
226	J045143.42+445733.8	72.931	44.959	160.758	0.458	0.23	74.31	3.34	16.98 ± 0.03	16.10 ± 0.03	15.62 ± 0.04	0.94	0.95	Irr	—
227	J044812.83+445407.6	72.053	44.902	160.404	-0.055	0.14	32.10	3.16	17.03 ± 0.04	16.17 ± 0.03	15.64 ± 0.04	0.84	1.03	ℓ S	—
228	J045038.65+445618.6	72.661	44.938	160.652	0.298	0.15	-86.90	2.79	17.02 ± 0.03	16.02 ± 0.03	15.65 ± 0.04	0.92	0.97	ℓ S	—
229	J045453.21+444522.8	73.722	44.756	161.270	0.764	0.22	48.70	3.10	17.01 ± 0.04	16.09 ± 0.03	15.70 ± 0.05	0.89	0.93	Irr	—
230	J044822.79+445528.2	72.095	44.925	160.406	-0.018	0.17	46.87	3.19	17.10 ± 0.04	16.22 ± 0.03	15.72 ± 0.05	0.84	1.02	Irr	—
231	J045144.68+455508.4	72.936	45.919	160.020	1.072	0.63	0.58	4.87	17.34 ± 0.04	16.23 ± 0.03	15.74 ± 0.05	1.16	1.09	ℓ S	—
232	J044706.85+453448.3	71.779	45.580	159.761	0.235	0.39	36.30	3.36	17.28 ± 0.04	16.31 ± 0.03	15.75 ± 0.04	1.25	0.99	ℓ S	4994
233	J044926.38+445450.8	72.360	44.914	160.534	0.119	0.57	59.34	4.18	17.10 ± 0.03	16.21 ± 0.03	15.75 ± 0.04	0.92	0.96	e S	—
234	J044930.28+443329.0	72.376	44.558	160.815	-0.101	0.51	-64.84	3.81	16.99 ± 0.03	16.12 ± 0.03	15.79 ± 0.05	0.76	0.87	ℓ S	—
235	J045109.62+450323.9	72.790	45.057	160.620	0.444	0.47	-35.74	3.64	17.15 ± 0.03	16.20 ± 0.03	15.79 ± 0.04	0.93	0.96	ℓ S	—
236	J045517.43+450155.5	73.823	45.032	161.100	0.993	0.28	47.83	3.35	17.13 ± 0.03	16.17 ± 0.03	15.79 ± 0.04	0.90	0.96	Irr	—
237	J045401.45+451107.1	73.506	45.185	160.841	0.916	0.03	-22.56	2.69	17.14 ± 0.03	16.20 ± 0.03	15.80 ± 0.04	0.96	0.93	Irr	—
238	J044452.40+443535.1	71.218	44.593	160.255	-0.707	0.13	-44.30	2.75	17.23 ± 0.04	16.27 ± 0.03	15.83 ± 0.05	1.01	0.97	Irr	—
239	J044936.24+450910.5	72.401	45.153	160.370	0.294	0.16	-26.71	2.74	17.24 ± 0.04	16.27 ± 0.03	15.84 ± 0.04	0.97	0.97	Irr	—

Table B – Continued

ID no.	Unique ID	RA	Dec	ℓ	b	ϵ_K	ϕ_K	r_{K20}	J_{K20}	H_{K20}	K_{K20}	$E(B-V)$	J^0-K^0	Type	v_{rad}
	ZoA	deg	deg	deg	deg		deg	"	mag	mag	mag	mag	mag		km s ⁻¹
(1)	(2)	(3)	(4)	(5)	(6)	(7)	(8)	(9)	(10)	(11)	(12)	(13)	(14)	(15)	(16)
240	J044727.80+444723.1	71.866	44.790	160.400	-0.230	0.68	-44.49	6.25	17.08 ± 0.04	16.32 ± 0.04	15.87 ± 0.07	0.88	0.83	Irr	7288
241	J044428.93+443630.5	71.121	44.608	160.197	-0.750	0.07	41.10	2.86	17.40 ± 0.04	16.46 ± 0.04	15.97 ± 0.06	1.06	0.96	Irr	—
242	J044746.91+453420.6	71.945	45.572	159.843	0.319	0.30	-41.46	3.09	17.48 ± 0.04	16.45 ± 0.03	15.99 ± 0.05	1.23	0.96	Irr	—
243	J045143.79+444623.9	72.932	44.773	160.902	0.341	0.45	43.24	3.42	17.32 ± 0.04	16.37 ± 0.03	16.02 ± 0.06	0.88	0.91	Irr	—
244	J044846.14+455955.0	72.192	45.999	159.628	0.725	0.34	29.77	3.04	17.61 ± 0.05	16.60 ± 0.04	16.10 ± 0.05	1.18	1.01	ℓ S	—
245	J044942.24+452830.7	72.426	45.475	160.134	0.514	0.07	-32.30	2.56	17.45 ± 0.04	16.49 ± 0.03	16.10 ± 0.05	1.04	0.90	Irr	—
246	J045533.75+445954.9	73.891	44.999	161.157	1.009	0.20	-60.40	2.72	17.44 ± 0.04	16.50 ± 0.03	16.10 ± 0.05	0.91	0.94	Irr	—
247	J045024.44+453101.5	72.602	45.517	160.181	0.636	0.11	-61.08	2.70	17.78 ± 0.05	16.77 ± 0.04	16.28 ± 0.07	1.16	1.00	Irr	—
248	J044758.33+440708.0	71.993	44.119	160.975	-0.593	0.53	-81.40	3.07	17.66 ± 0.04	16.84 ± 0.04	16.38 ± 0.06	0.64	1.00	ℓ S	—
249	J044644.16+442005.1	71.684	44.335	160.667	-0.623	0.56	-74.98	3.12	17.66 ± 0.04	16.81 ± 0.04	16.47 ± 0.07	0.73	0.88	m S	5654
250	J044602.99+445836.4	71.512	44.977	160.099	-0.299	0.33	-63.40	3.07	17.87 ± 0.05	17.24 ± 0.05	16.47 ± 0.07	0.96	0.99	Irr	—
251	J045222.42+450342.7	73.093	45.062	160.752	0.612	0.33	-74.00	2.64	18.03 ± 0.05	17.02 ± 0.04	16.57 ± 0.07	0.91	1.07	Irr	—
252	J045430.84+444644.9	73.628	44.779	161.211	0.727	0.68	5.66	2.85	18.45 ± 0.06	17.50 ± 0.05	17.08 ± 0.09	0.88	0.99	ℓ S	—
253	J045302.36+454133.4	73.260	45.693	160.338	1.102	0.74	-73.61	3.78	18.56 ± 0.06	17.68 ± 0.05	17.09 ± 0.08	1.11	1.00	Irr	—
254	J044817.36+445352.2	72.072	44.898	160.416	-0.048	0.95	-33.50	11.71	18.42 ± 0.09	17.67 ± 0.09	17.17 ± 0.15	0.84	0.89	Irr	—
255	J045034.26+435930.6	72.643	43.992	161.370	-0.320	0.60	-48.07	2.10	19.24 ± 0.10	18.93 ± 0.13	17.81 ± 0.13	0.64	1.16	Irr	5724
256	J044602.10+443424.5	71.509	44.573	160.400	-0.560	0.05	68.79	1.51	19.00 ± 0.11	18.07 ± 0.09	17.85 ± 0.19	0.94	0.74	Irr	6281
257	J045426.93+444941.5	73.612	44.828	161.170	0.750	0.24	69.67	1.38	19.29 ± 0.09	18.44 ± 0.08	18.05 ± 0.15	0.89	0.85	Irr	5072
258	J045217.47+450839.9	73.073	45.144	160.680	0.650	0.56	43.93	1.78	19.72 ± 0.11	18.84 ± 0.09	18.27 ± 0.15	0.87	1.07	Irr	6680
259	J044644.76+444734.7	71.687	44.793	160.320	-0.320	0.19	75.89	0.94	19.83 ± 0.12	18.84 ± 0.09	18.80 ± 0.24	0.89	0.65	Irr	5709
260	J044838.16+454506.4	72.159	45.752	159.800	0.550	0.35	-77.10	1.07	21.83 ± 0.74	19.89 ± 0.27	18.96 ± 0.24	1.14	2.37	Irr	5745
261	J045026.76+451130.7	72.612	45.192	160.440	0.430	0.63	-53.75	0.73	21.77 ± 0.35	20.25 ± 0.17	20.07 ± 0.39	1.02	1.26	Irr	4639

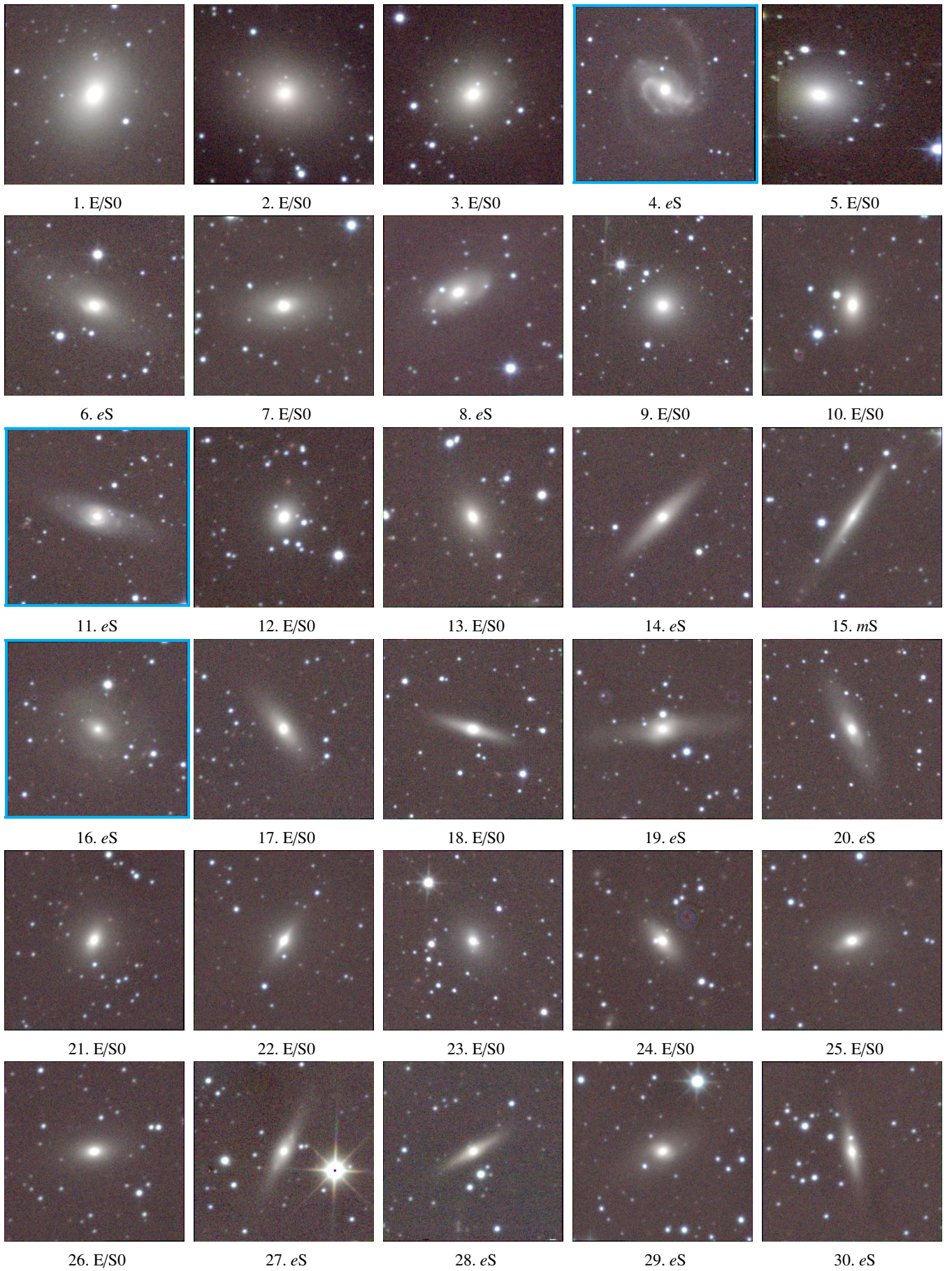


Figure B. The false-colour – J (blue), H (green) and K (red) representation ($1.2' \times 1.2'$) of galaxy candidates of the 3C 129 cluster. The cyan frames indicate H I detection in the WSRT H I-survey.

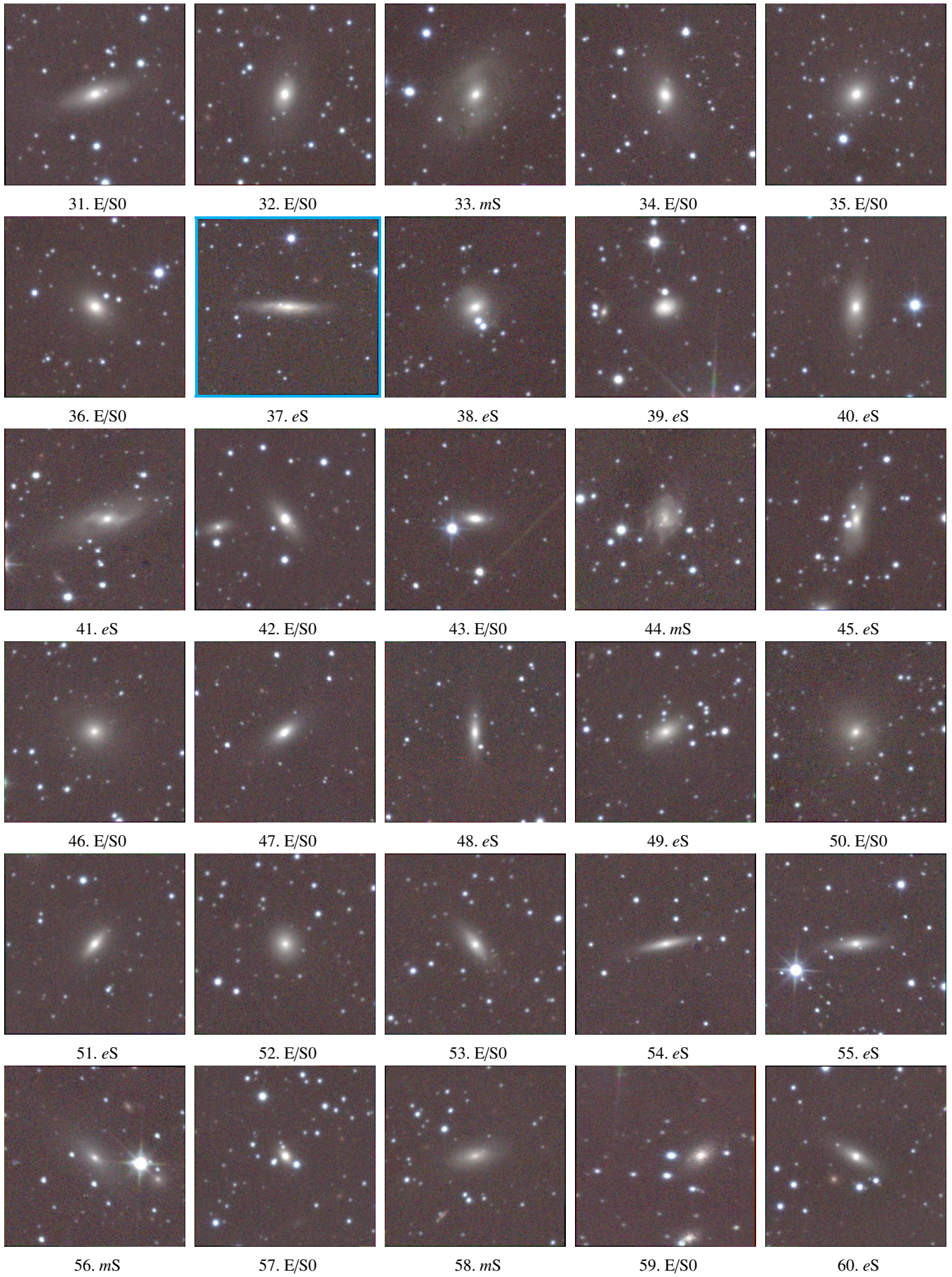


Figure B – Continued.

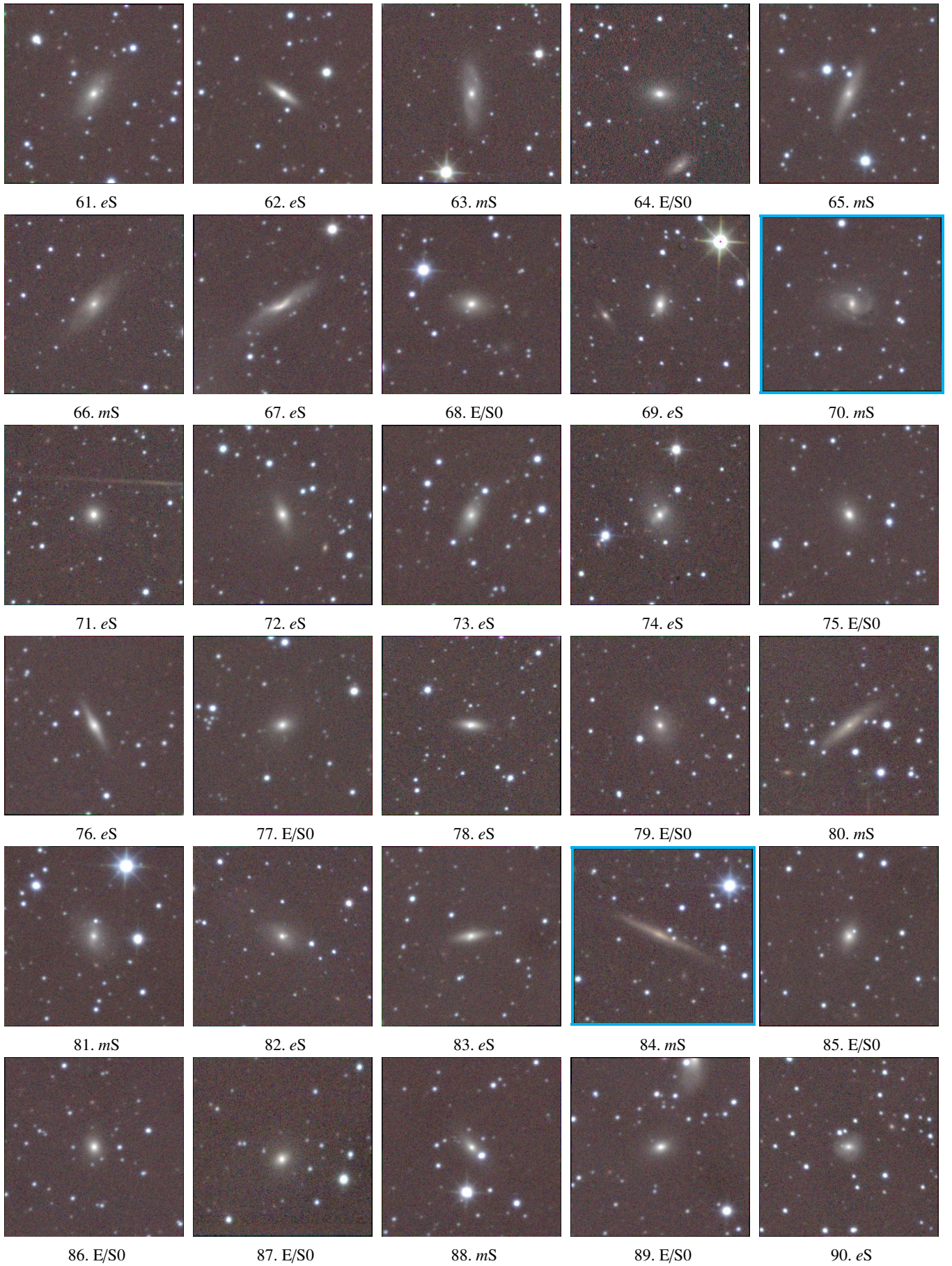


Figure B – Continued.

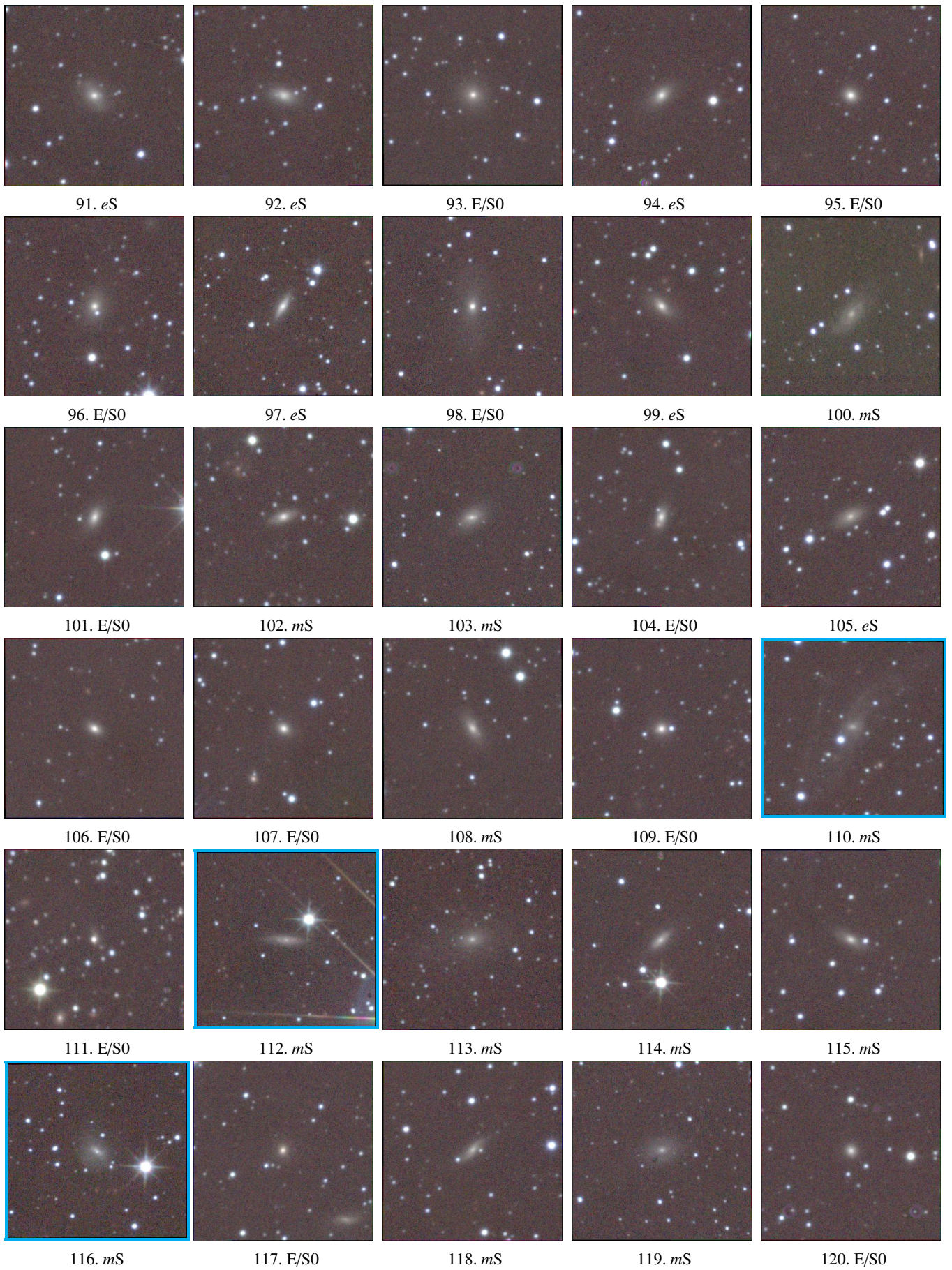


Figure B – Continued.

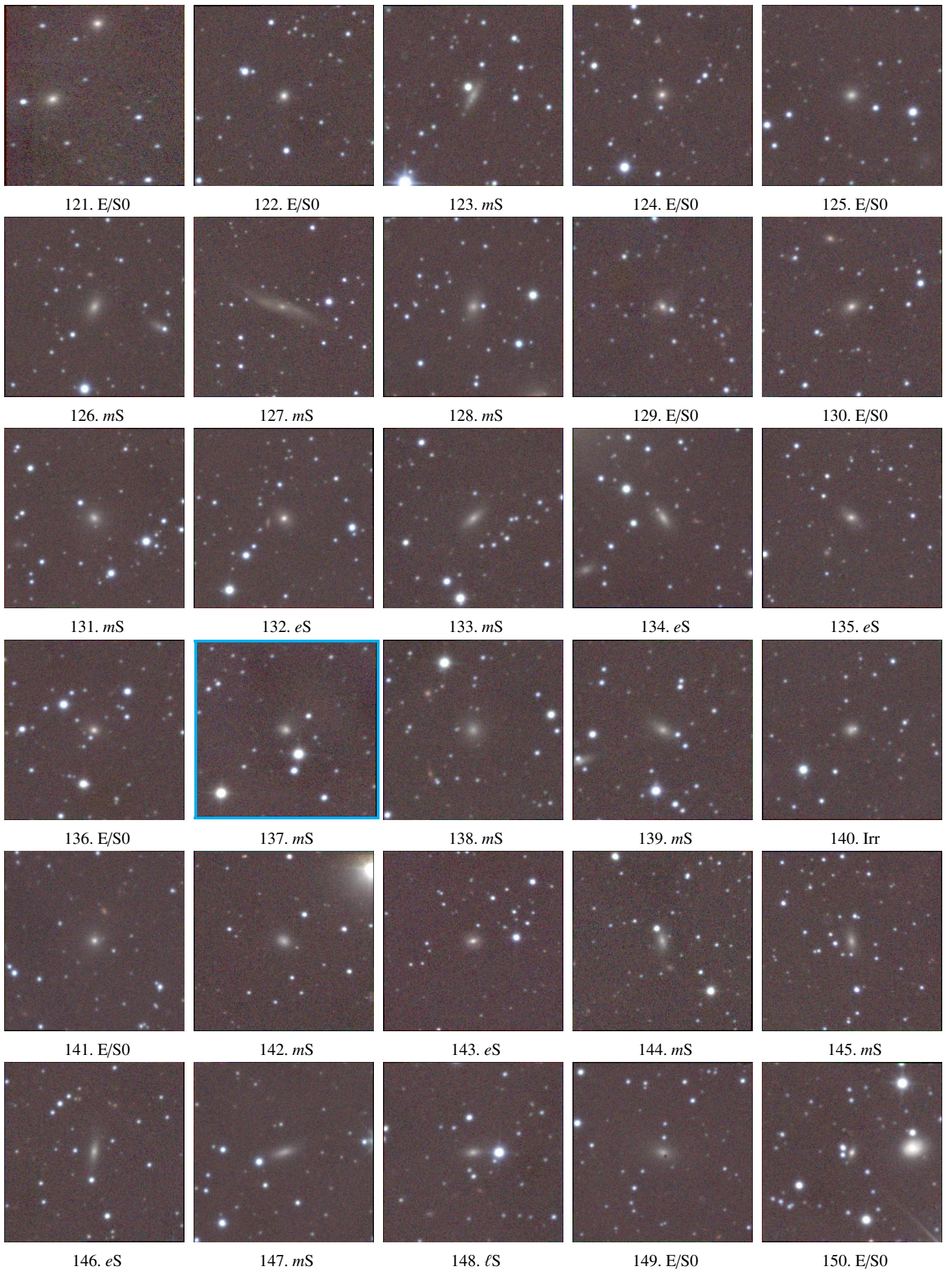


Figure B – Continued.

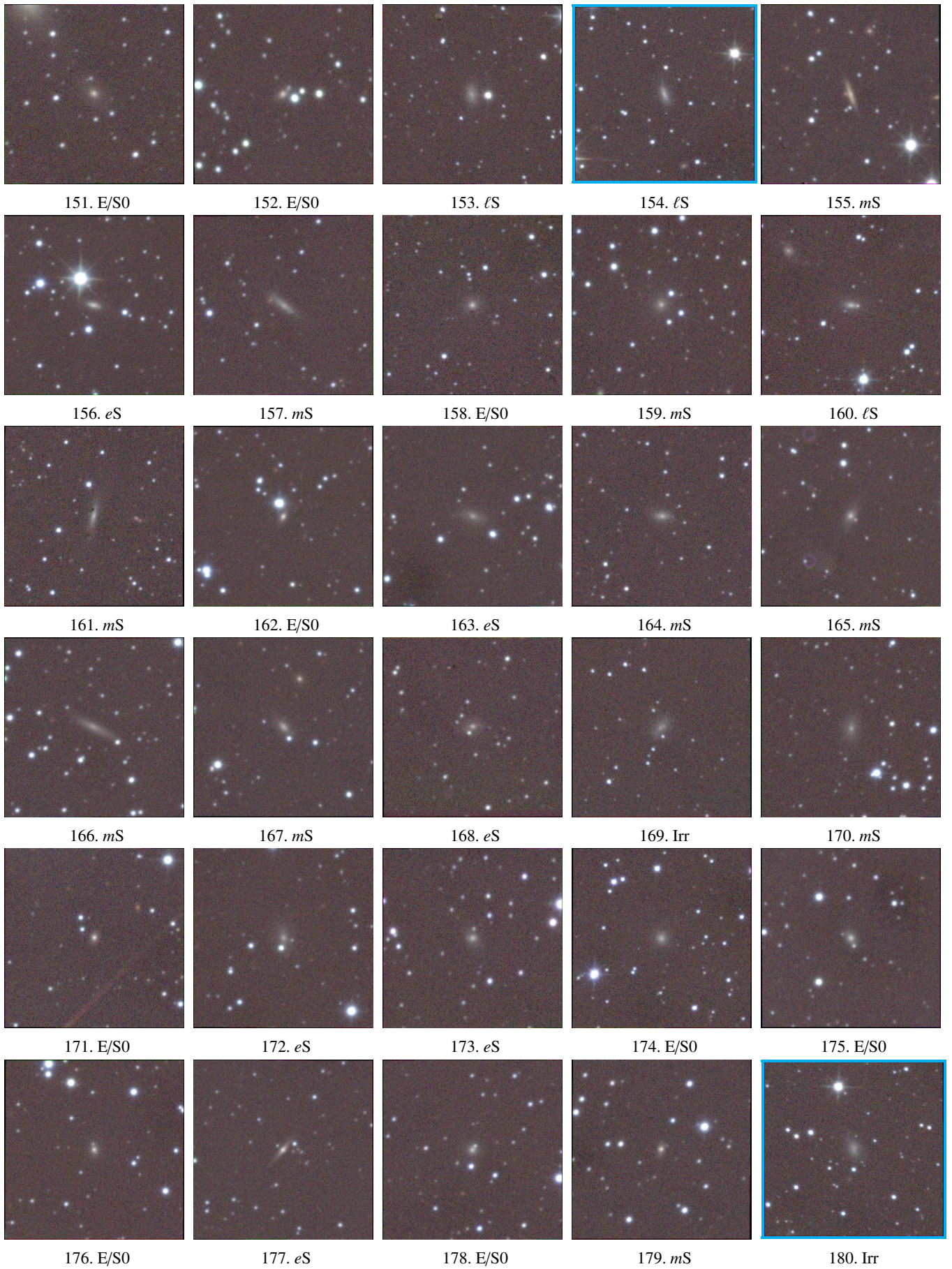


Figure B – Continued.

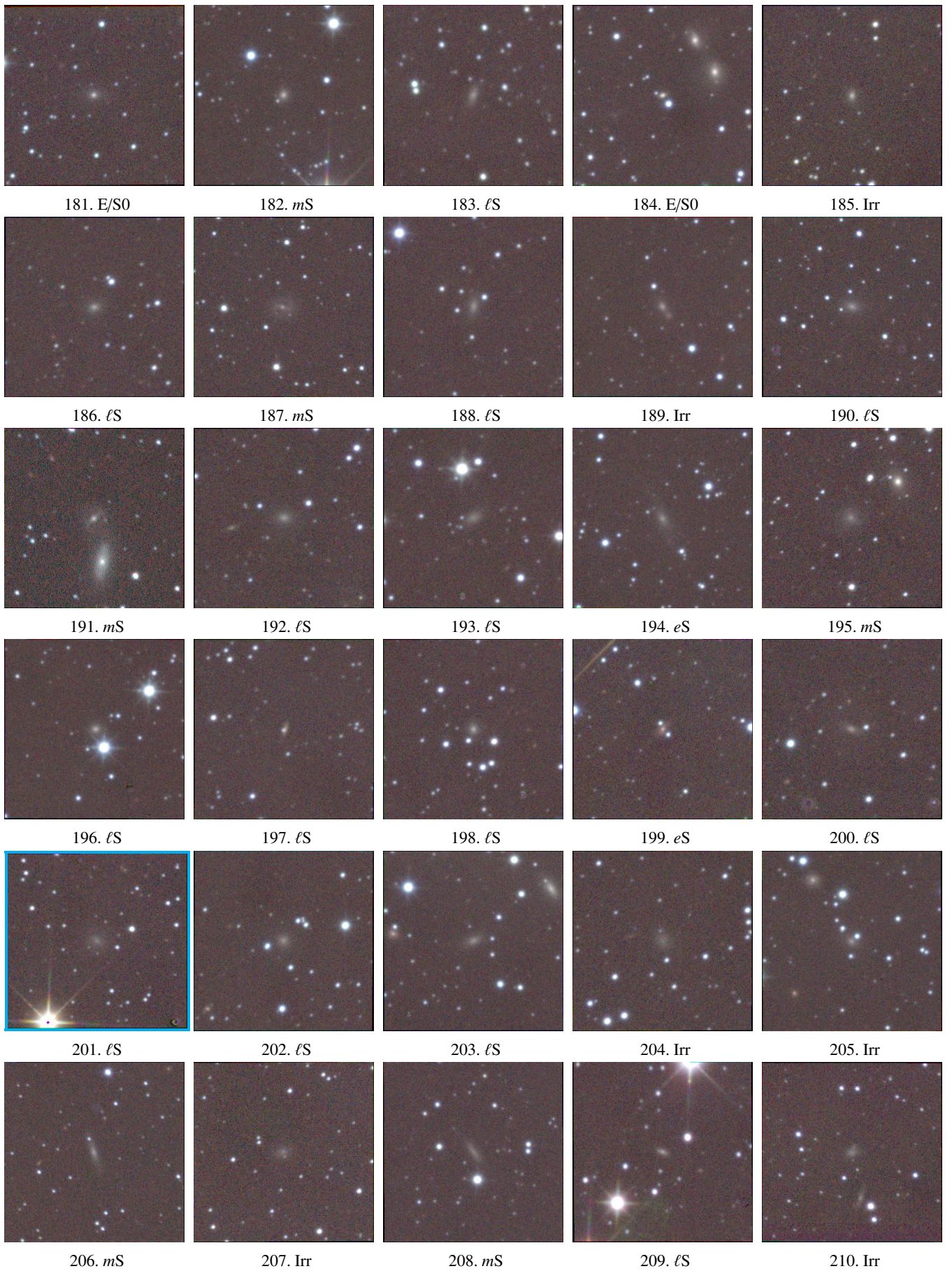


Figure B – Continued.

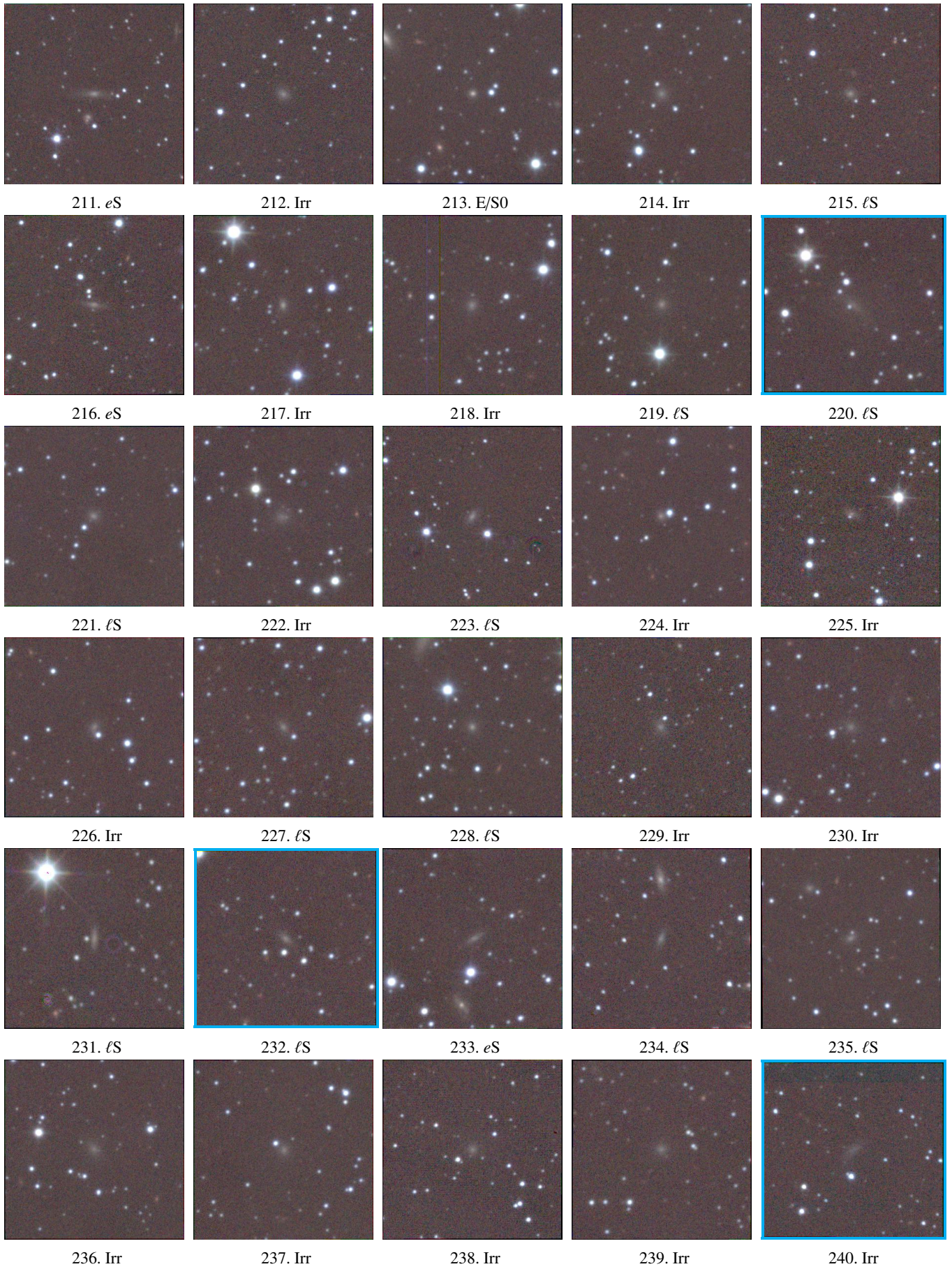


Figure B – Continued.

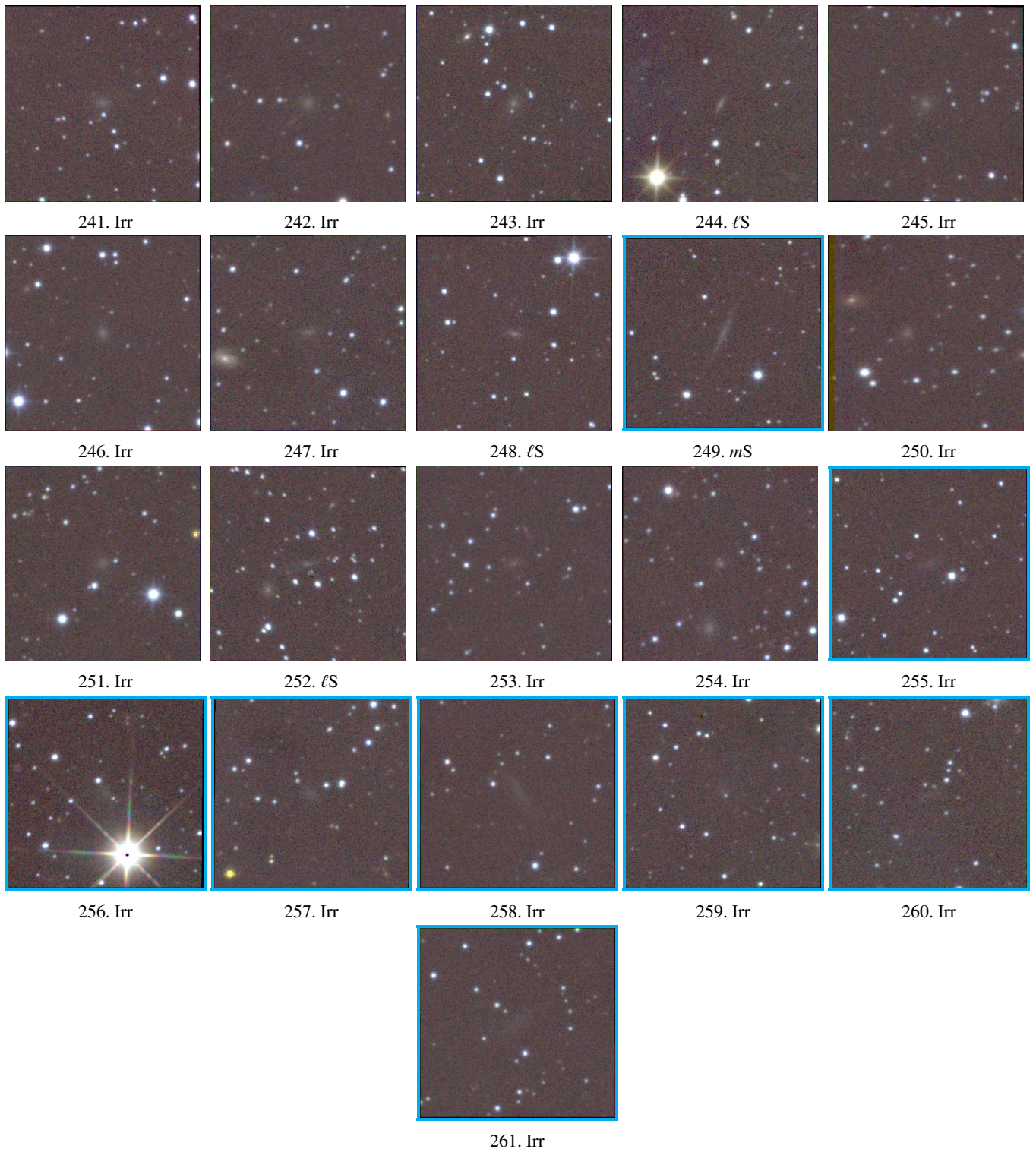


Figure B – Continued.